

**Generalized Interpolation applied to
MR Image Magnification and Gradient
Nonlinearity Correction**

by

Zachary W. Slavens, B.S.

A Thesis submitted to the Faculty
of the Graduate School,
Marquette University,
in Partial Fulfillment of
the Requirements for
the Degree of
Master of Science

Milwaukee, Wisconsin
May 2008

Preface

Post processing of magnetic resonance (MR) images generally make use of cubic interpolation to estimate values off of the Cartesian grid, as it does not suffer from the artifacts caused by linear and nearest neighbor interpolation yet is not as computationally expensive as sinc interpolation. In this thesis, we look to investigate whether recent advances in generalized interpolation techniques can be extended to improve MR image quality, while keeping in mind the relative computation cost of competing techniques. We start with head to head comparisons of interpolation techniques on compounded rotations of controlled, simulated data. Next, the impact on phantom and in-vivo data sets when this higher order interpolant is used along with complex data in image magnification is demonstrated. Finally, the non-rigid transformation mapping of MR gradient distortion correction is considered and how this separable one-dimensional technique from the prior chapters and references behaves when extended to a non-separable application.

Acknowledgements

I would like to acknowledge the guidance and support from my committee throughout the course of this thesis, Dr. Polzin, Dr. Johnson and Dr. Richie. The encouragement from family and friends has been very important to me, especially from my wife, Brooke, and parents, Bill and Sue. Thank you.

Table of Contents

1. Introduction.....	1
1.1. Overview of MR.....	3
1.2. Overview of Gradient Nonlinearity Correction.....	5
1.3. Overview of Interpolation.....	10
1.4. Overview of Generalized Interpolation.....	12
2. Simulated Results.....	16
2.1. Introduction.....	16
2.2. Methods.....	16
2.3. Results.....	20
2.4. Discussion and Conclusion.....	24
3. Application to MR Image Magnification.....	26
3.1. Introduction.....	26
3.2. Methods.....	26
3.3. Results.....	29
3.3.1 Phantom Results.....	31
3.3.2 In-vivo Results.....	33
3.4. Discussion and Conclusion.....	33
4. Application to MR Gradient Non-linearity Correction.....	35
4.1. Introduction.....	35
4.2. Methods.....	36
4.2.1. Separability.....	36
4.2.2. Forward-Inverse Distortion Correction.....	37
4.2.3. Error Measurement.....	38

4.2.4. Data Collection	39
4.3. Results.....	40
4.4 Discussion and Conclusion.....	48
5. Summary	50
5.1. Discussion & Conclusion.....	50
5.2. Future Work	50
6. References.....	55
7. Appendix.....	58

1. Introduction

Magnetic Resonance Imaging (MRI) scanners started to become part of clinical radiology practice in the early 1980s. As an imaging modality, MRI is comparable to X-ray Computed Tomography (CT) in its ability to measure cross-sections of anatomy. They differ in what is being imaged however. While x-rays are sensitive only to changes in electron density, MR is mostly used to measure hydrogen, as humans are made up mostly of water and fat, each molecule consisting of hydrogen. The MR scanner is capable of manipulating tissue contrast by weighting images to be representative of proton density, transverse and longitudinal relaxation rates. Beyond measuring the amount of signal in tissue, the complex acquired data can be used for phase sensitive applications, such as flow and fat-water imaging.

In 1983, US Patent 4,591,789 [1] was issued for the image processing technique to correct for nonuniformity in the MRI gradient subsystem needed for spatial localization. Described is the use of a separable low order polynomial interpolation scheme as it performs a better approximation than nearest neighbor and linear and does not have the high compute time of sinc, the optimal solution. Also described are hardware alternatives for which implementation is undesirably complicated and expensive. These limitations still exist and the post-processing correction is still used by MR vendors to date. Around the same time, 1981, the cubic interpolation kernel was described [2] as a piecewise polynomial well suited for applications, being better than linear approximation at a low compute cost. In the paper, this Cubic Keys interpolant for resampling a 64x64 image to 350x336 took about 17 seconds.

More recently a group of papers [3-5] have been published addressing the image quality versus computation time tradeoff made with interpolants. They propose using a generalized interpolation strategy with a fast prefiltering step to get higher quality approximations in a short amount of time. From this framework, functions are derived from B-splines which provides a maximum approximation order with a minimum support interpolant. Cubic interpolation is still used today in many digital image processing applications related to MR such as console interaction with data and gradient nonuniformity correction. This recent work combined with advances in computer speed serve as motivation to revisit the interpolation strategies being used today.

This thesis looks to investigate whether new advances in approximation techniques can be extended to improve quality of post-processing done on MR data over today's norm of using cubic interpolation, and to acknowledge the relative computational burden of the technique for the particular application. The remainder of this chapter will build the background needed to examine the three core portions of the thesis. The second chapter evaluates the performance of one generalized interpolant against the cubic and a 16-point apodized sinc for the case of compounded rotations. Next, Chapter Three looks at the impact on phantom and in-vivo data sets when this higher order interpolant is used with complex data in image magnification. Chapter Four considers the non-rigid transformation mapping of gradient distortion correction and how this separable one-dimensional technique from the prior chapters and references behaves when extended to a non-separable application.

1.1. Overview of MR

Magnetic resonance (MR) is a noninvasive imaging modality that uses a large electromagnet to produce a magnetic flux density (B_0) along the z-axis, as shown in Figure 1, generally on the order of 1.5 Tesla (T) or 3.0 T for full body clinical scanners. When nuclei are exposed to B_0 , they combine to have a net polarization along the longitudinal axis, parallel to the direction of B_0 , also called the z-axis. The hydrogen will exhibit resonance at a known frequency proportional to B_0 according to the Larmor Equation,

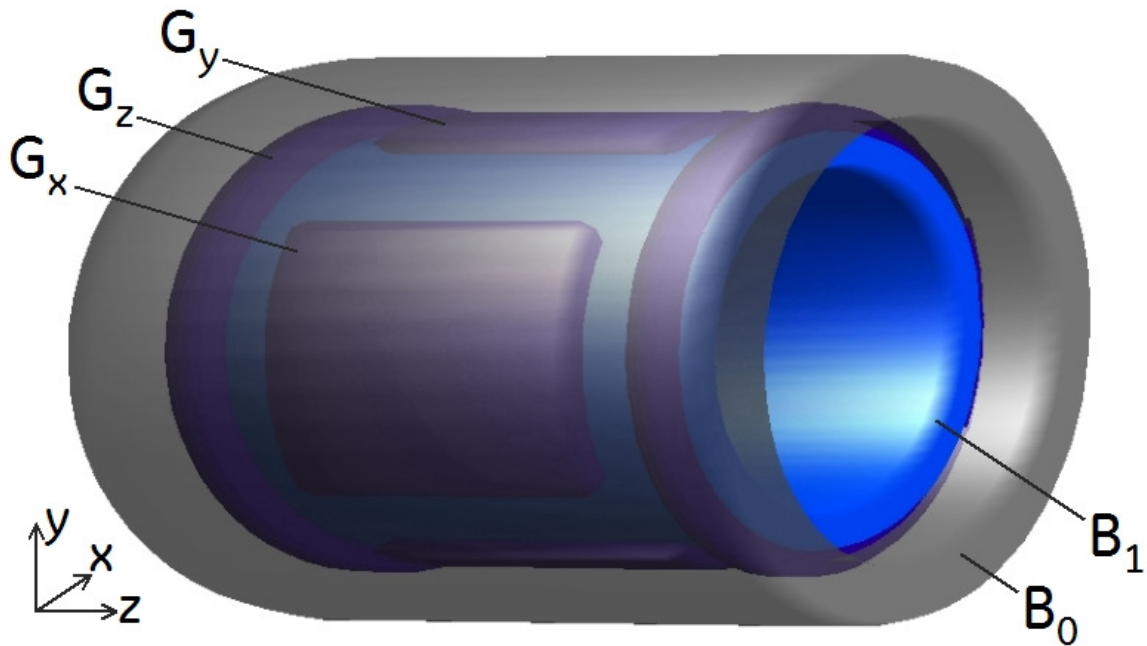


Figure 1. Cartoon depicting the static electromagnet, radiofrequency and gradient coils.

$$f = \frac{\gamma}{2\pi} B. \quad (1.1)$$

Where $\frac{\gamma}{2\pi} = 42.58$ MHz per Tesla, so that, for example, at 1.5 T and 3.0 T would oscillate at approximately 64 MHz and 128 MHz respectively. [6]

A radiofrequency magnetic pulse (B_1) is applied perpendicular to the z-axis to excite these precessing hydrogen nuclei into the transverse plane. After B_1 is turned off, the direction in which the hydrogen nuclei point will cease to be tipped into the transverse plane and will begin to go back to equilibrium. The exponential rate of regrowth along the longitudinal axis is called T_1 , and T_2 describes the decay in the transverse plane. A receive coil can be positioned such that the rotating transverse magnetization vectors induce a signal.

This describes how an object can generate a signal, but when all the processing is at the same frequency we are unable to determine where in space the signal originates. For spatial localization, gradients (G_x, G_y, G_z) are used to vary the magnetic field along the corresponding axis, and as an example for the x-axis with $B_z = B_0$,

$$G_x = \frac{\partial B_z}{\partial x}. \quad (1.2)$$

While B_0 is specified in Tesla, G is generally referred to in Gauss/cm or mTesla/m. For example, turning on G_x would change (1.1) to be

$$f = \frac{\gamma}{2\pi} (B + G_x x) \quad (1.3)$$

From this, it can be seen that this variable magnetic field will cause different rates of precession, and these varying frequency components can be used to map to a specific location via the Fourier Transform in reconstruction processing. While this mapping is assumed to be linear, it is not actually so throughout the entire imaging volume.

1.2. Overview of Gradient Nonlinearity Correction

As mentioned in Section 1.1, patent [1] describes a separable 1D distortion and intensity correction of pixel data to correct for non-uniformities in the gradient system. Two hardware options are also mentioned for improving nonlinearity. The first of these is widening of the bore to increase the effective linear region, which is expensive and also requires that the power required to drive the gradients increases proportionally to diameter raised to the 5th power. A second is to design gradient coils with higher order correction current, however this additional coil inductance would again increase gradient drive power and require more complicated coil construction. Noted in the patent is that at least a quadratic order polynomial should be used to trade off the significant blurring from nearest neighbor or linear interpolation with the time-consuming but higher quality sinc-interpolation, and in practice a cubic convolution kernel was used to do so.

Using 5th order polynomials to represent each G_x , G_y and G_z , one can compute the distortion error $\epsilon(x, y, z)$ for each axis as a function of location in space where (1.3) becomes

$$f = \frac{\gamma}{2\pi} (B + G_x(x + \epsilon_x(x, y, z))). \quad (1.4)$$

Figure 2 shows the absolute error in cm for a 48cm field of view (FOV) within a TwinSpeed gradient coil set in whole-mode for each axis as well as the total error. It can be seen from the color maps that there is very little error (less than 1cm) at the center portion of the FOV, but over 6cm of position error toward the FOV extremities.

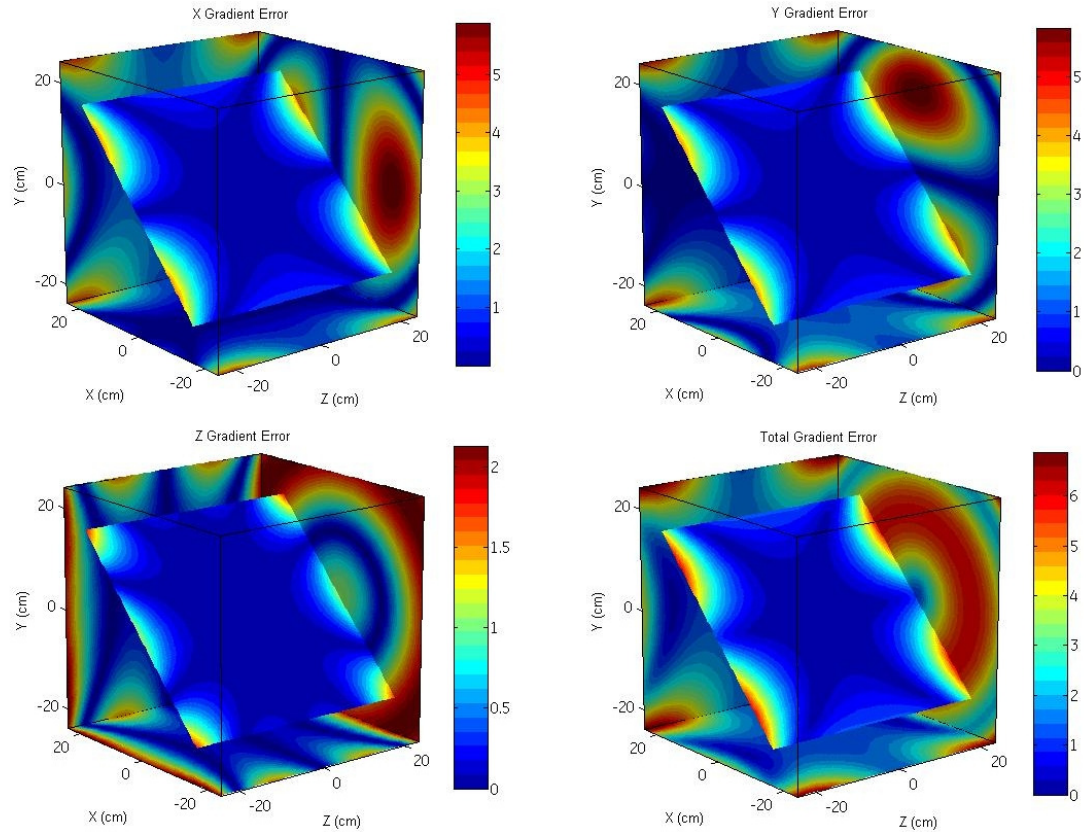


Figure 2. Gradient error as a function of position in centimeters within a 48cm field of view.

Aside from correcting for displacement, there also needs to be a correction for the signal contained within a distorted voxel as shown in Figure 3b, given that the density of tissue imaged is not proportional to that of nondistorted, rectangular voxels as in Figure 3a.

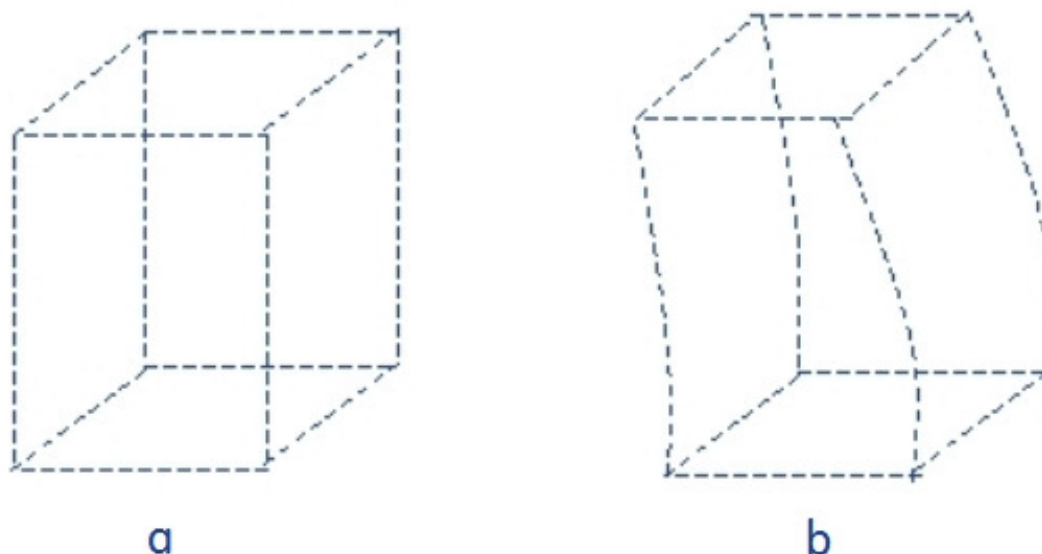


Figure 3. (a): Nondistorted voxel. (b): Distorted voxel.

While the above technique covers a broad range of MR imaging scenarios, a 1995 patent was issued [7] to utilize both real and imaginary signal components in the correction for phase images used for phase contrast angiography and flow velocity measurements. The reason for performing this correction separately on the real and imaginary components of the complex signal is to avoid the situation where an interpolated neighborhood includes a $\pm\pi$ boundary. A pure interpolation of radians would give the incorrect result of phase being nearly zero, whereas the complex interpolation correctly estimates around $\pm\pi$. Shown in Figure 4 is an example where complex data has been convolved with a boxcar and the resulting phase is plotted (Figure 4b) versus the boxcar averaging of the phase only (Figure 4c) which has errors due to phase wrap.

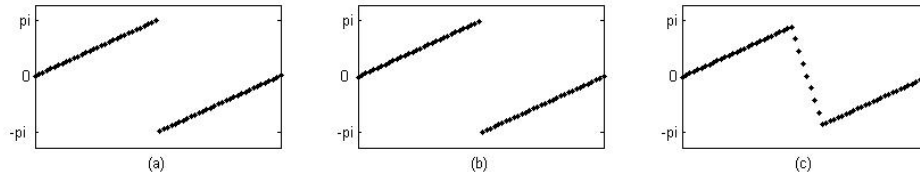


Figure 4. (a) Phase plot of original complex data. (b) Phase plot of boxcar smoothed complex data. (c) Plot of boxcar smoothed phase, with errors in the center from the $\pm\pi$ boundary.

Considering other applications, continuously moving the patient table during acquisitions has been shown to extend the field of view (FOV) from 30cm to 150cm along the z-direction for peripheral vascular run-offs [8]. The potential of this technique for MR Angiography (MRA) comes with the cost of each object measurement being made at slightly different locations with respect to the gradients. Here the spatial dependent blurring was corrected for by separately performing gradient error correction on each individually reconstructed phase encode line and summing together all of these resulting complex images. This idea is extended beyond this multi-step correction in [9], where the gradient error is embedded into the exponential term Fourier transform.

As a practical example of what standard gradient non-linearity does to an MR image, a phantom consisting of three parallel grids (Figure 5) was imaged on EchoSpeed gradients (GE Healthcare, Waukesha, WI). The phantom was inserted into the bore of the magnet so that three 48cm FOV coronal slices were acquired and saved with gradient nonlinearity correction disabled. These uncorrected slices have been textured mapped to gradient iso-contours in (Figure 6) as described in [10]. Note that the central slice, at isocenter along the Y-axis, has little through-plane curvature, while the two slices 10cm away start to have enough curvature that at the edges along the Z-axis they begin to leave the grid phantom altogether.



Figure 5. Phantom consisting of three parallel grids.

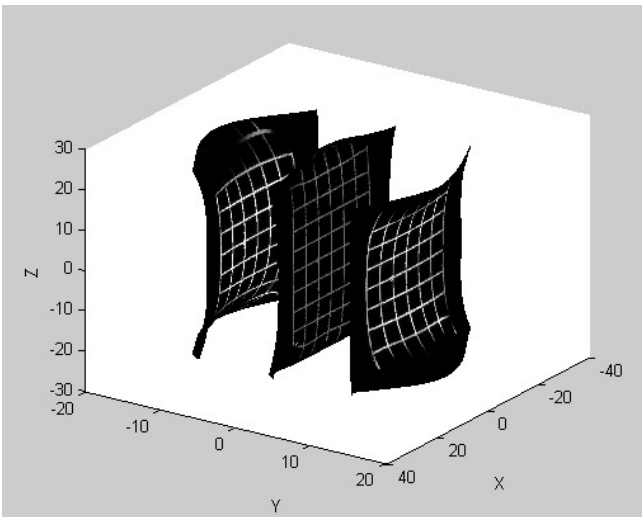


Figure 6. Grid phantom images texture mapped to gradient iso-contours.

Another way of seeing the impact of the correction is to view the uncorrected grid phantom image shown in Figure 7 next to the corrected image shown in Figure 8.

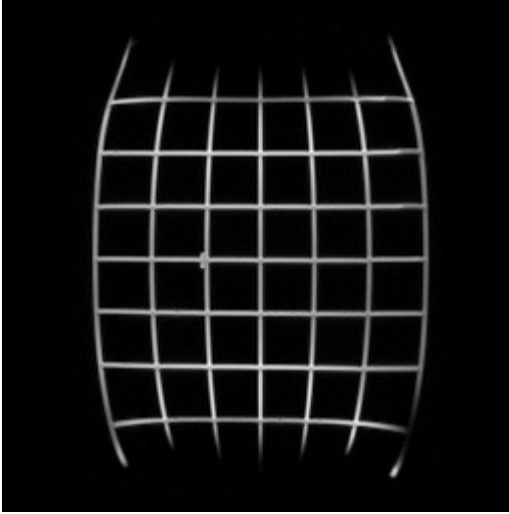


Figure 7. Uncorrected slice of grid phantom.

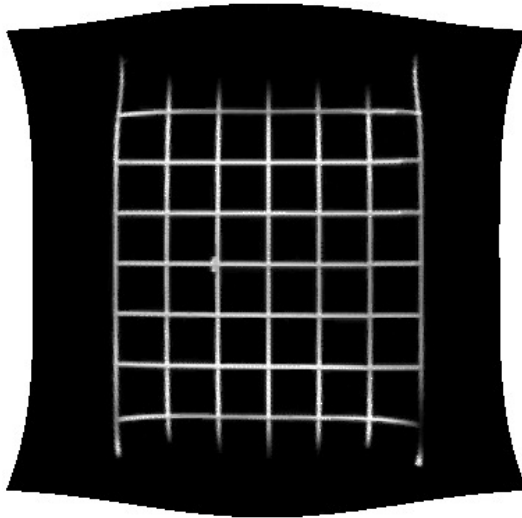


Figure 8. Corrected slice of grid phantom.

1.3. Overview of Interpolation

Just before the time the first gradient nonuniformity correction patent was issued, Robert Keys described a cubic convolution interpolation,

$$cubic_keys(x) = \begin{cases} (a+2)|x|^3 - (a+3)|x|^2 + 1, & 0 \leq |x| < 1 \\ a|x|^3 - 5a|x|^2 + 8a|x| - 4a, & 1 \leq |x| < 2 \end{cases} \quad (1.5)$$

that could be used for digital image processing and applied it separably to two dimensional images [2]. As an example, Figure 9 shows this function when $a = -1.0$, and described in an image resampling comparison [11] as a high-resolution cubic spline with edge enhancement. This is of particular interest, as this function is used for gradient distortion correction.

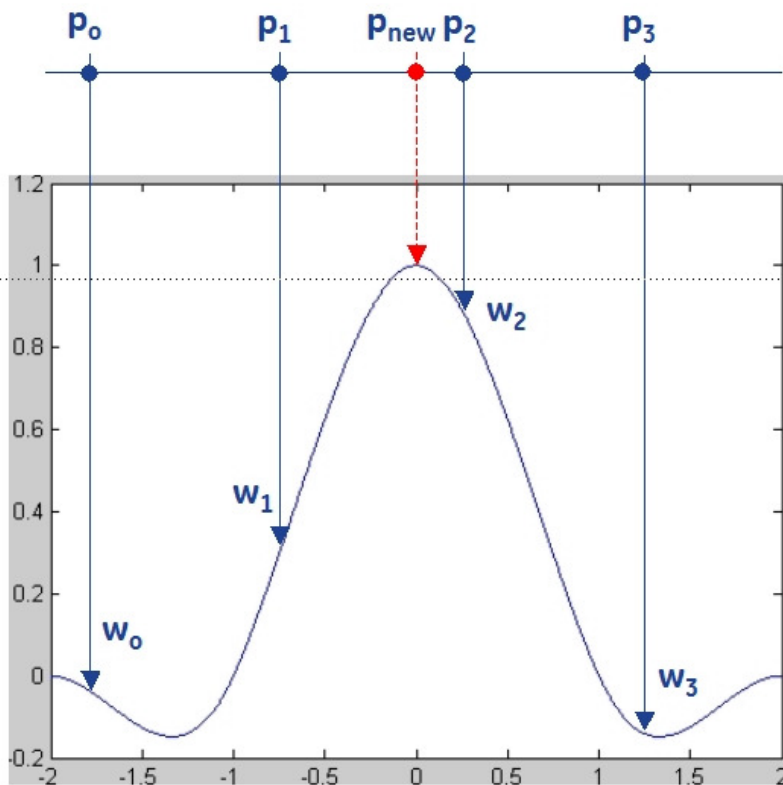


Figure 9. Example of a single point being estimated from a Cubic Keys (-1.0) interpolant.

Consider the case of estimating point p_{new} of a one dimensional output array from an input array location which is not on the Cartesian grid. Using the four-point cubic interpolation and referring to Figure 9, the input value at p_0 is multiplied by the weighting value w_0 , and similarly for p_1 , p_2 and p_3 by w_1 , w_2 and w_3 , respectively. The

result of these multiplications are then summed together to provide an estimate for p_{new} that is stored in the output array. This procedure can be extended to image processing by performing this operation along each axis individually. If this procedure is going to be done often, a lookup table can be used to store the weights once and save computing them each time.

1.4. Overview of Generalized Interpolation

The Biomedical Imaging Group in Switzerland, has published a group of papers [3-5] addressing the image quality versus computation time tradeoff made with interpolants. With standard image interpolation, a neighborhood of pixels f_k are directly weighted by an interpolant φ_{int} and combined to form the new image

$$f(x) = \sum_{k \in Z} f_k \varphi_{int}(x - k). \quad (1.6)$$

Instead of being constrained to interpolating actual pixel values, interpolant coefficients c_k which represent those values are then used to form the final output

$$f(x) = \sum_{k \in Z} c_k \varphi(x - k). \quad (1.7)$$

This technique is called generalized interpolation and gives freedom for potentially fast implementation of interpolants with large support. The block diagram below in Figure 10 shows the steps involved in going from input discrete signal (f_{in}) to coefficients (c) and finally to output interpolated signal (f_{out}).

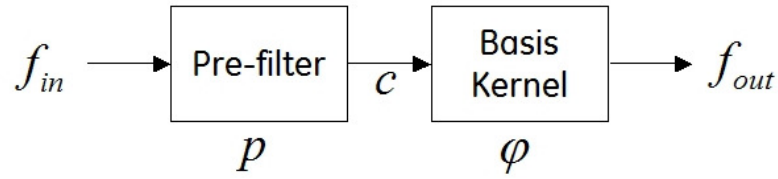


Figure 10. Block diagram of generalized interpolation.

The basis function (φ) is convolved with the coefficients to determine the output signal, and generally has similar shape to standard interpolants with low-pass behavior. The pre-filter is designed specifically with φ in mind. For example, if φ is an finite impulse response (FIR) linear phase filter with zeros at -0.67 and -1.5 , then the infinite impulse response (IIR) pre-filter will have poles at -0.67 and -1.5 . It has been demonstrated [5,12,13] that this prefilter can be implemented very efficiently as an in-place causal filter with $M = Length - 1$,

$$c[n] = \begin{cases} \sum_{n=0}^M c[n](z^n + z^{M-n}), & n = 0 \\ c[n] + zc[n-1] & , 1 \leq n \leq M \end{cases} \quad (1.8)$$

followed by an anti-causal filter,

$$c[n] = \begin{cases} \frac{z^2 c[M] c[M-1]}{z^2 - 1}, & n = M \\ z(c[n+1] - c[n]), & 0 \leq n \leq M - 1 \end{cases} \quad (1.9)$$

From this, one could view interpolation as a special case of this generalized framework where the pre-filter is a delta function (δ) leading to $c = f_{in}$.

From this framework a class of functions were designed [3,4] to have maximum order with minimum support (MOMS). Through linear combinations of same-order B-

splines and their derivatives, o-MOMS are optimized to have the largest approximation order for a given amount of support. As an example, a cubic B-spline, given as:

$$B^3(x) = \begin{cases} \frac{2}{3} - \frac{1}{2}|x|^2 (2 - |x|), & 0 \leq |x| < 1 \\ \frac{1}{6}(2 - |x|)^3 & , 1 \leq |x| < 2 \end{cases} \quad (1.10)$$

and the derived cubic o-MOMS function given as:

$$oMOMS^3(x) = B^3(x) + \frac{1}{42} \frac{d^2}{dx^2} B^3(x) = \begin{cases} \frac{1}{2}|x|^3 - |x|^2 + \frac{1}{14}|x| + \frac{13}{21} & 0 \leq |x| < 1 \\ -\frac{1}{6}|x|^3 + |x|^2 - \frac{85}{42}|x| + \frac{29}{21} & 1 \leq |x| < 2 \end{cases} \quad (1.11)$$

has the same amount of support as the cubic Key's function described in (1.5).

The first curiosity of this function is that if the output is equal to the input, there is a 13/29 scaling at the point of interest and non-zero scaling at other integer values. This differs from the cubic and sinc functions discussed so far which have a scaling of 1 for the point of interest and scaling of zero elsewhere. Here we apply this generalized interpolation scheme to a Dirac impulse (Figure 11) and a rectangle function (Figure 12) in order to demonstrate the behavior of the prefilter and show that for the case where the output resides directly on the same Cartesian grid as the input that the two are in fact equivalent.

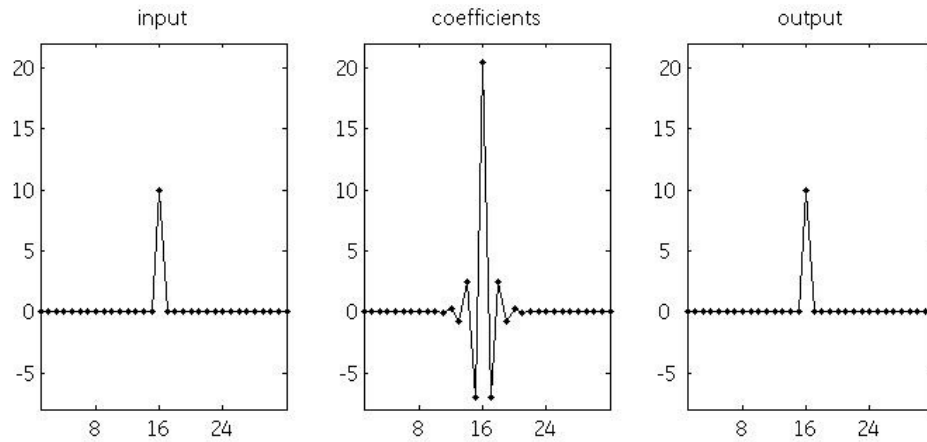


Figure 11. Application of cubic oMOMS to a Dirac impulse, showing the intermediate prefiltered coefficients and the final output.

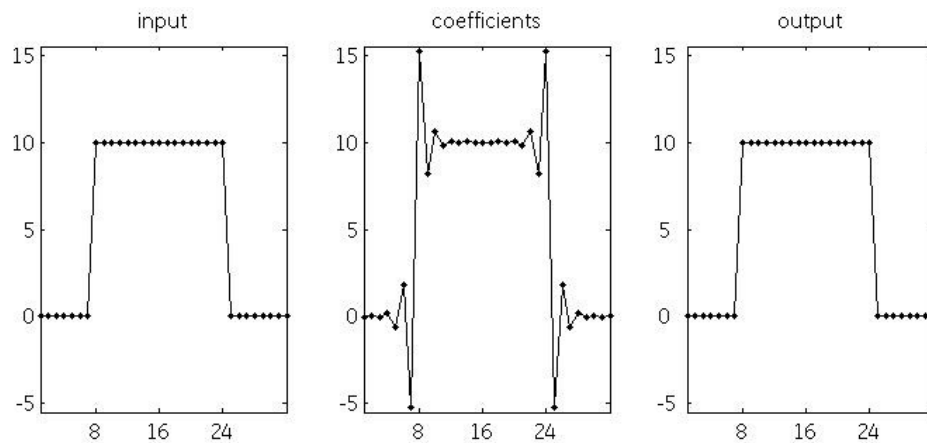


Figure 12. Application of cubic oMOMS to a rectangle function, showing the intermediate prefiltered coefficients and the final output.

In the following chapter, this technique is extended as simulated phantoms are used to visually exploit different characteristics of the interpolation schemes when applied to identical transformations. Following this, the application of generalized interpolation to image magnification is evaluated on phantom and in-vivo data, along with the possibility of leveraging the complex data available with MRI. Finally, the correction scheme for gradient non-linearity is implemented to apply what has been learned above along with the impact of separability to this non-rigid body transformation.

2. Simulated Results

2.1. Introduction

Scanner data can be very complicated in practice, even phantom data with control for physiological motion will contain noise, partial volume effects, and phase errors due to receiver delays and magnet inhomogeneity. While it is important to eventually apply algorithms to acquired scanner data, exercising them on synthetic data can control for these practical imaging issues and provide a starting point to compare the different interpolation techniques in isolation. In this chapter we will create simulated phantom data and perform transformations using a variety of algorithms for interpolation.

2.2. Methods

The first synthetic phantom used in this work, shown in Figure 13, is a bullseye pattern created from a sinusoid propagating from the center of the image out to the edges, similar to a pattern used in the original Keys' paper [2] and the later Blu [4] and Thevanez [5] work, with the exception that a two-pixel wide line is added extending from the center out to one side of the image. This will be referred to as the Bullseye Phantom. The other phantoms were designed specifically to reveal how well each interpolation technique maintained resolution and the amount of ringing that resulted since these two are generally competing properties of an image that are impacted from filter design. The simulated points data shown in Figure 14 is a binary image with the bright points spaced every five pixels along the horizontal and vertical axis, and will be called the Points Phantom. The simulated lines image shown in Figure 15 consists of a pair of one-pixel wide horizontal lines, a pair of one-pixel wide vertical lines and a one-pixel wide

diagonal line, and is referred to as the Lines Phantom. All of the figures shown below are the center half of the image that is actually rotated to avoid the contribution from the corners of a square image being rotated off the side during circular rotation. This is also true of any measurements made.

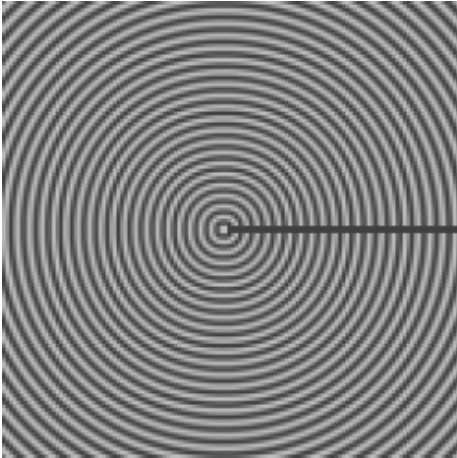


Figure 13. Simulated Bullseye Data

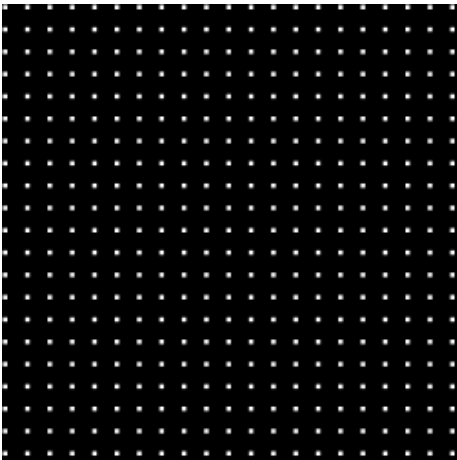


Figure 14. Simulated Points Data

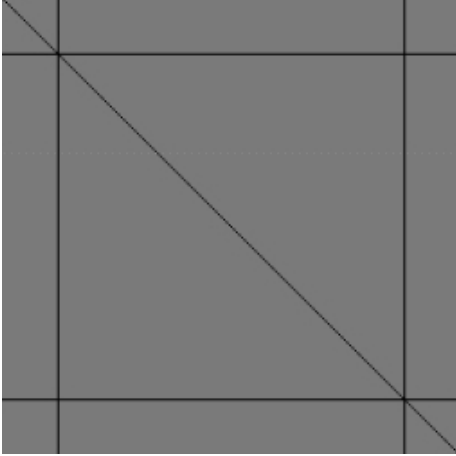


Figure 15. Simulated Lines Data

Three interpolation methods are evaluated here: a Keys cubic, a cubic o-MOMS and a 16-point apodized sinc. The purpose is to determine how the generalized interpolation scheme compares against the commonly used four point cubic convolution kernel, as well as an apodized sinc function with a much larger support of 16. The motivation for evaluating the cubic convolution is that it is what is used today for gradient non-linearity correction and often for console image manipulation. The much larger sinc interpolation is chosen to be a higher order interpolant to compare the smaller kernels, and provide high quality interpolation, despite being considerably more intense, computationally. The cubic convolution kernel is a Keys' function with $\alpha = -1.0$ resulting in an interpolant described by

$$y(x) = \begin{cases} |x|^3 - 2|x|^2 + 1 & 0 \leq |x| < 1 \\ -|x|^3 + 5|x|^2 - 8|x| + 4 & 1 \leq |x| < 2 \end{cases} \quad (1.12)$$

Matching the support of this is the cubic o-MOMS generalized interpolant,

$$y(x) = \begin{cases} \frac{1}{2}|x|^3 - |x|^2 + \frac{1}{14}|x| + \frac{13}{21} & 0 \leq |x| < 1 \\ -\frac{1}{6}|x|^3 + |x|^2 - \frac{85}{42}|x| + \frac{29}{21} & 1 \leq |x| < 2 \end{cases} \quad (1.13)$$

with pre-filter pole at $\frac{\sqrt{105}-13}{8}$, which is approximately -0.344 .

The final method for interpolation considered uses a 16-point sinc function apodized with a Kaiser-Bessel window [14]. Kaiser used a modified Bessel function of the first kind to approximate the optimal solution to balance mainlobe width to sidelobe gain [15], resulting in this weighting function where β defines the window shape, $(M+1)$ is the window length, $\alpha = (M+1)/2$, and $I_0(\bullet)$ represents the zeroth order modified Bessel function of the first kind:

$$w[n] = \begin{cases} \frac{I_0[\beta(1-[(n-\alpha)/\alpha]^2)^{1/2}]}{I_0(\beta)} & , 0 \leq n \leq M \\ 0 & , \text{otherwise} \end{cases} \quad (1.14)$$

For this experiment $\beta = 3.0$, which scales the center of the sinc by 1.0 and the tails by 0.2. This window was meant to baseline how the other methods compared to a much more expensive sinc interpolation kernel that is generally regarded to provide high quality interpolation.

Based on a method similar to those used in [4,5,16] for determining interpolation quality, each synthetic phantom and interpolation method was rotated by 18 degrees clockwise 20 times for a total of 360 degrees. The output of one rotation would be the input to the next rotation in order to visually reveal the compounding effects that each function has on the image. This does not translate directly into an application as the

original data would be used independent of rotation angle, but does give a gross view of the subtle differences between the competing schemes.

2.3. Results

The rotations line up exactly with the original image so that a quantitative measurement can be made for comparison. The final image (g) and original image (f) are evaluated pixel by pixel via a metric used in [5]

$$figmerit = 10 \log \left(\frac{\sum_{x,y=1}^{len_{x,y}} f_{x,y}^2}{\sum_{x,y=1}^{len_{x,y}} (f_{x,y} - g_{x,y})^2} \right). \quad (1.15)$$

This figure of merit has a numerator that is a fixed reference for each data set and has a denominator which decreases as the observed and expected results near, so that large values show a better approximation. If a transform is so accurate that $f_{x,y} = g_{x,y}$, this figure of merit will be equal to infinity. Also note that if errors become large and cause the denominator to be larger than the numerator then the log will cause the figure of merit to be negative. This occurs for the cubic interpolant used in the bullseye and points phantom (Figure 16), but not for the lines phantom which is predominantly flat with little global opportunity for blurring. The cubic oMOMS interpolation performs the best overall for the bullseye phantom and nearly as well as the 16-point apodized sinc, which performs best with respect to this metric for the points and lines phantom. Next, the qualitative assessment of image quality for each phantom is shown.

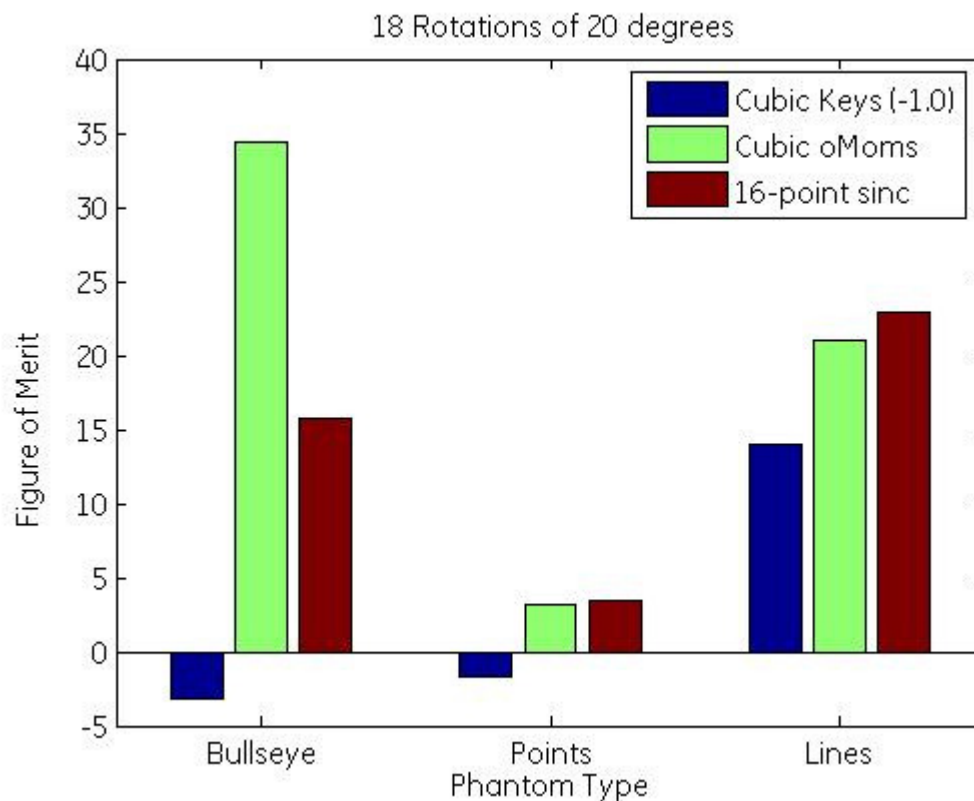


Figure 16. Likeness of interpolation scheme after compounded rotations to original data.

Figure 17a illustrates the effect on the bullseye phantom from compounded rotations with the four-point cubic Keys function. It can be seen that errors concentrate more towards the center of the bullseye. The line extending out from the center is blurred from the low-pass nature of the function. Results of the rotating experiment with the four-point cubic oMOMS, shown in Figure 17b, and 16-point apodized sinc shown in Figure 17c, show each retained the bullseye pattern and line without significant blurring.

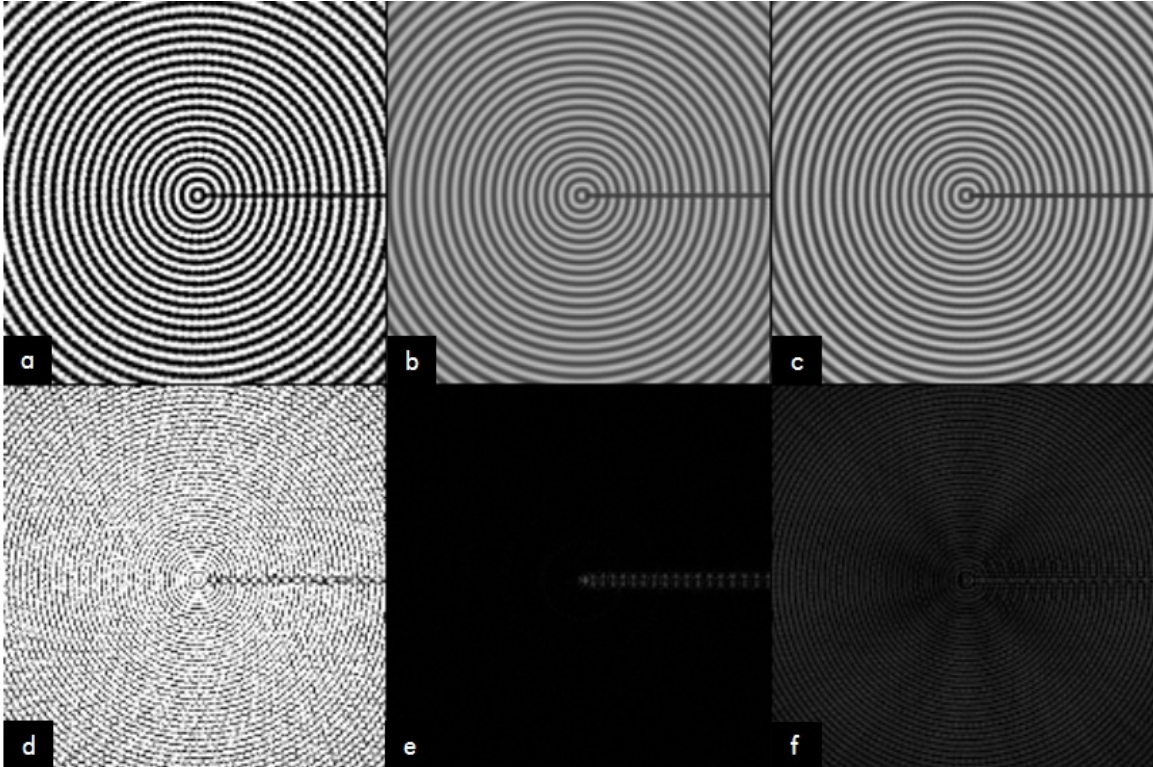


Figure 17. Bullseye Phantom. Rotated with (a) cubic, (b) cubic oMOMS and (c) 16-point apodized sinc. Absolute difference (d-f) between original image and top (a-c) results.

Results from the resolution experiment using the compounded rotations of the simulated points phantom and shown in Figure 18a-c, where the identical window-width, window-level is used. The cubic Keys function causes spreading of the single point to a large enough neighborhood where some points have been blurred together. Similarly, but to a lesser degree, the cubic oMOMS interpolation spreads the single pixel into a neighborhood of 4-6 pixels Figure 18b. Blurring was slightly less with the 16-point apodized sinc in the neighborhood directly surrounding the original single pixel, but there was small background signal scattered throughout the image from the slowly decaying shape of the sinc function.

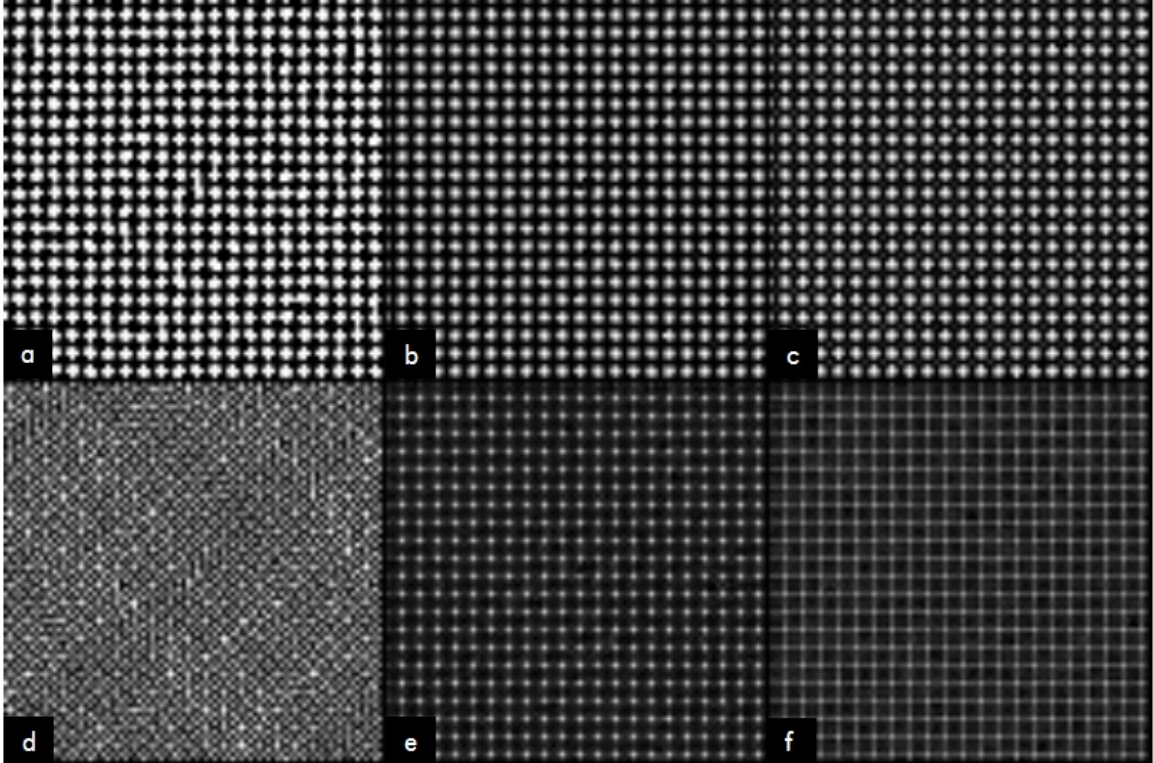


Figure 18. Points Phantom. Rotated with (a) cubic, (b) cubic oMOMS and (c) 16-point apodized sinc. Absolute difference (d-f) between original image and top (a-c) results.

Results from the rotated lines phantom shown in Figure 19, cubic convolution shows artifact along the long abrupt discontinuities in the simulated data made up of a diagonal, horizontal and vertical. Cubic oMOMS (Figure 19b) has slight broadening of the dark line with a small amount ringing of to each side of the line edges. Significant ringing is present propagating off of each line from the 16-point apodized sinc along with a general background texture across the entire image arising from the slowly decaying interpolant. Despite these shortcomings, the apodized sinc has the least amount of broadening of the black lines, most easily seen horizontal and vertical lines in the difference image (Figure 19f) where the very center is black, or small difference.

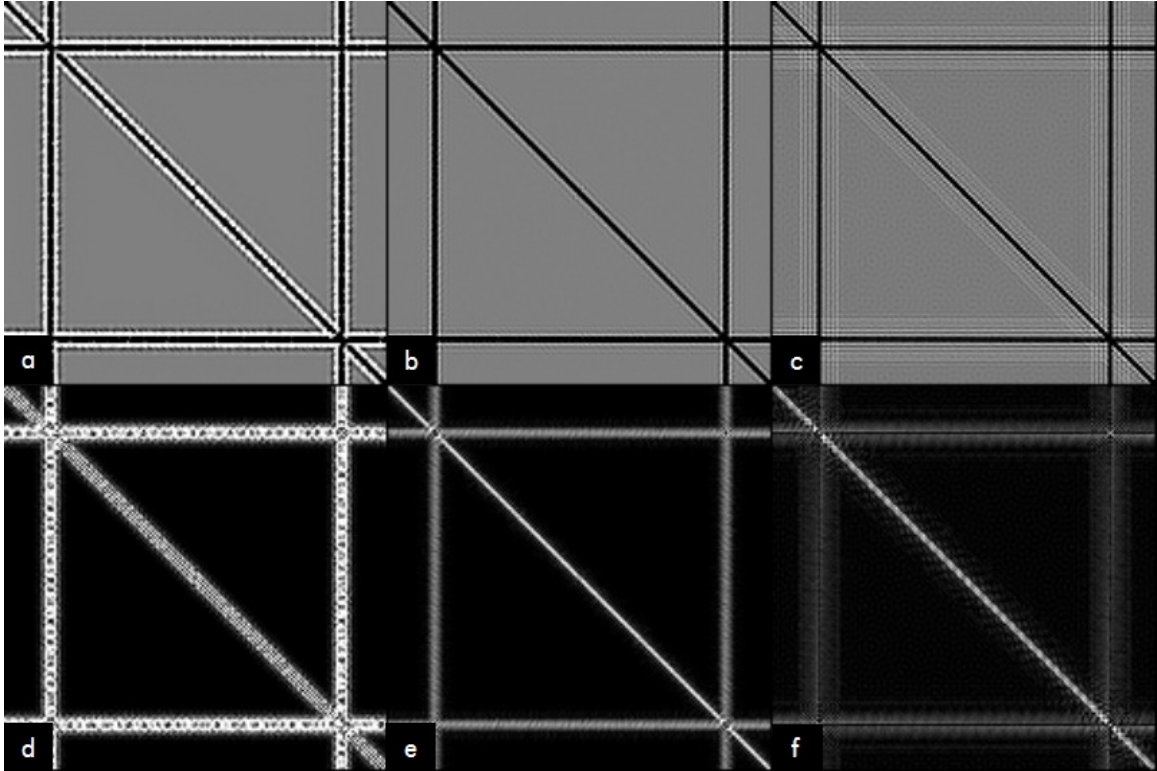


Figure 19. Lines Phantom. Rotated with (a) cubic, (b) cubic oMOMS and (c) 16-point apodized sinc. Absolute difference (d-f) between original image and top (a-c) results.

2.4. Discussion and Conclusion

Anticipated results for these experiments were that the overall image quality from the generalized interpolant would fall partly in between the four-point and 16-point interpolants, nearing the cubic interpolant given their more similar compute intensity. However, the cubic oMOMS generally provided an approximated image very similar to the original, rivaling the larger support sinc interpolant in two cases and surpassing it in one. It is known that a sinc interpolant of infinite extent is the ideal interpolant, but this experiment also shows the challenge of truncating the support of the ideal sinc function, even when using windowing to reduce the associated oscillatory behavior.

Analyzing the computation cost, the fastest of the three kernels evaluated is the Cubic Keys. Due to the pre-filtering step, the cubic oMOMS needs 1.75 times the compute time and the 16-point sinc takes 4 times. As an alternative way of looking at the earlier figure of merit plot in Figure 16, Figure 20 shows this data normalized by the compute complexity of each interpolant. For all simulated phantoms, the cubic oMOMS has higher performance per computation than the 16-point apodized sinc. The best performing method per computation cost for the lines phantom, which is predominantly flat with little structure, is the cubic Keys. Given the relatively low computation cost and image quality in the simulated data experiments with the generalized interpolation scheme, extending the experiments to actual MR data looks to give promising results.

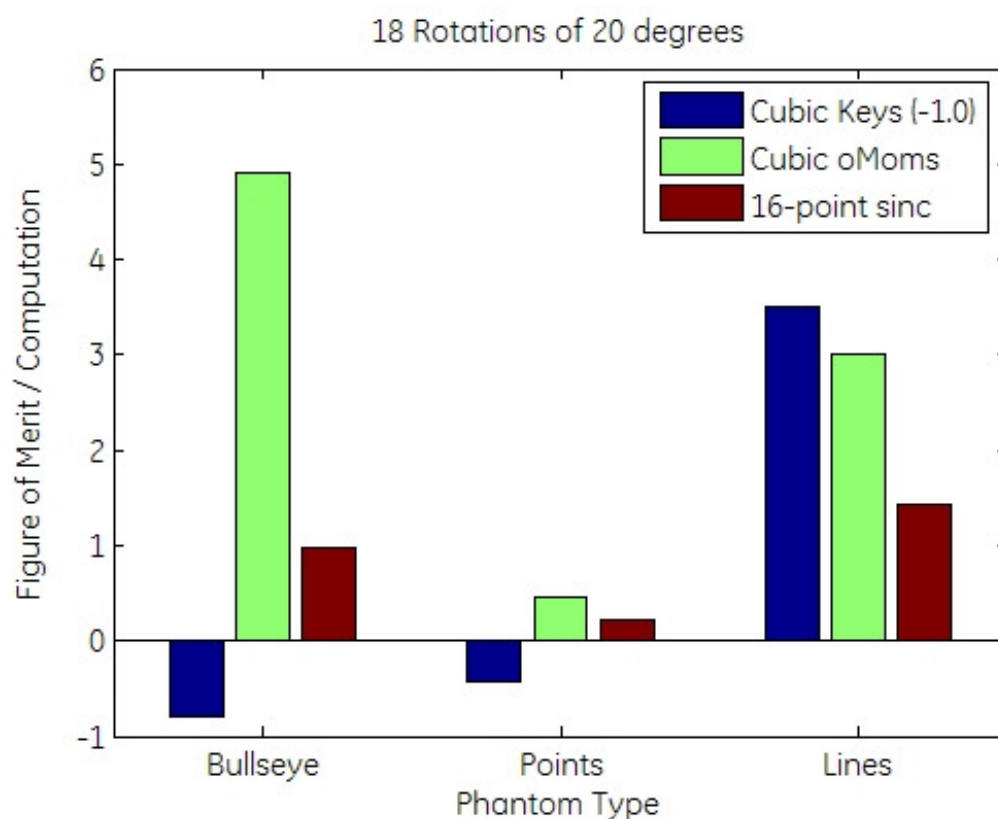


Figure 20. Likeness of interpolation scheme after compounded rotations to original data normalized to the computation cost of each interpolant.

3. Application to MR Image Magnification

3.1. Introduction

During image viewing and manipulation of images on MR scanners and workstations, magnification is commonly used along with rotation and shifting of the data for closer inspection. When an image is pulled out of a database and interaction with this data requires information to be made available off of the Cartesian grid, interpolation is used to determine the missing information. A cubic interpolation kernel is often used because it does not suffer from the same artifacts that can be caused by nearest neighbor or linear interpolation, while still being small enough in size to be computationally reasonable. This limited kernel support can still have a low-pass effect on the image however. Because of this, image reconstructions often zero-pad acquired k-space data and insert what is equivalent to a sinc-interpolated image into the database. Evaluated here is an alternative where an acquired-size, complex image is made available to the display and generalized interpolation is used on this data for improved spatial resolution. An abstract to this work [17] is in the Appendix.

3.2. Methods

To quantify the overall impact of the interpolation procedures described below, each image is magnified by a factor ranging from 1.1 to 4.0 times the original x and y dimensions in increments of 0.1. For example, a 256x256 image magnified by 1.5 in this experiment will yield a 384x384 image. As MR reconstruction often provides zero-padded DFT-based interpolated images today, this will be used as a standard of reference to compare against. The sinc interpolation method as applied to MR image magnification

is discussed in [18]. Two interpolation kernels will be considered, the first is Keys cubic convolution [2] with $\alpha = -1.0$,

$$y(x) = \begin{cases} |x|^3 - 2|x|^2 + 1 & , 0 \leq |x| < 1 \\ -|x|^3 + 5|x|^2 - 8|x| + 4 & , 1 \leq |x| < 2 \end{cases} \quad (1.16)$$

which, implemented separably, requires eight multiply-adds per pixel of the output image.

The second is a generalized interpolation method that involves pre-filtering of the image data, followed by interpolation of the filtered image. From a category of functions that give maximal order interpolation for a minimal amount of support (MOMS)[4], the four-point cubic o-MOMS [4] function is used as the interpolant,

$$y(x) = \begin{cases} \frac{1}{2}|x|^3 - |x|^2 + \frac{1}{14}|x| + \frac{13}{21} & , 0 \leq |x| < 1 \\ -\frac{1}{6}|x|^3 + |x|^2 - \frac{85}{42}|x| + \frac{29}{21} & , 1 \leq |x| < 2 \end{cases} \quad (1.17)$$

The pre-filter applied is specifically designed for use with this interpolant and is well described in [5]. Due to the equivalent support, the compute time for both methods are the same with exception of the additional pre-filtering step in the o-MOMS processing, which becomes negligible as the size of the magnified image increases. Only two-dimensional magnification is performed in this particular chapter, but the techniques can be extended to any number of dimensions. Figure 21 shows the additional cost of the prefiltering step associated with this 4-point interpolant. Since the prefiltering is performed on the input data, it is not subject to the amount of compute scaling the interpolation step is exposed to when a particular axis is being magnified. The

interpolant step performs four floating-point multiplies and three adds and the prefiltering step takes three multiplies and two adds.

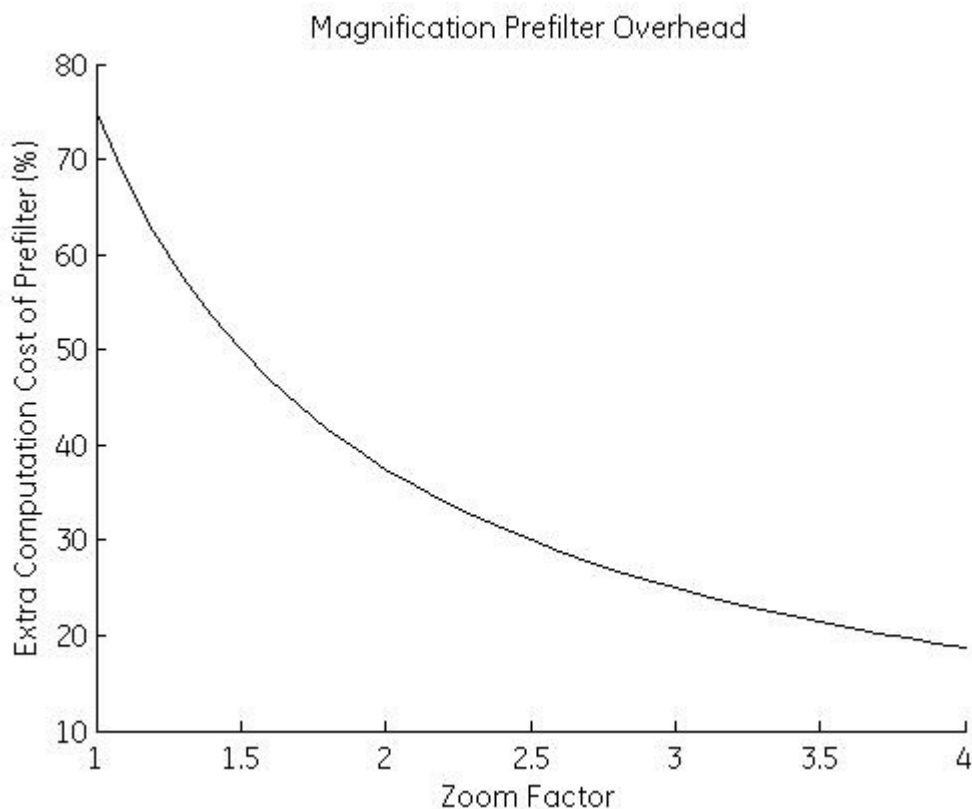


Figure 21. Additional cost of the prefiltering stage over cubic interpolation.

In addition to the interpolation functions considered above, the impact of performing magnification on the magnitude image versus the magnification of real and imaginary components separately is compared. The interpolation time will take twice as long for this complex case.

All data was collected from a GE Signa HDx 1.5 T scanner with EchoSpeed gradients (GE Healthcare, Waukesha, WI, United States). A single channel head coil was used to acquire 256x256 matrix of the American College of Radiology (ACR) phantom (Fig 1a) and a T1-weighted brain (Fig 2a) data. Abdomen data (Fig 3a) was acquired with

an eight-channel torso array at a 320x192 matrix size. Ahn-Cho phase correction [19] was performed on each coil before the complex coil summation. The phase information would otherwise be completely removed with a sum of squares multi-channel coil combination.

3.3. Results

For each magnification performed, a measurement was made on the final magnitude image using (1.15) to evaluate how well the result of an interpolation experiment (g) corresponds to the expected result [5], which in this case is the image from zero-padded interpolation (f). For the cases where the real and imaginary components are interpolated separately, the magnitude of each complex pixel is computed before equation (1.15) is evaluated.

This figure of merit has a numerator has a fixed reference for each data set and has a denominator which decreases as the observed and expected results near, so that large values show a better approximation.

Figure 22 shows the mean of this figure of merit across the range of magnifications (1.1 to 4.0x) for each interpolation type.

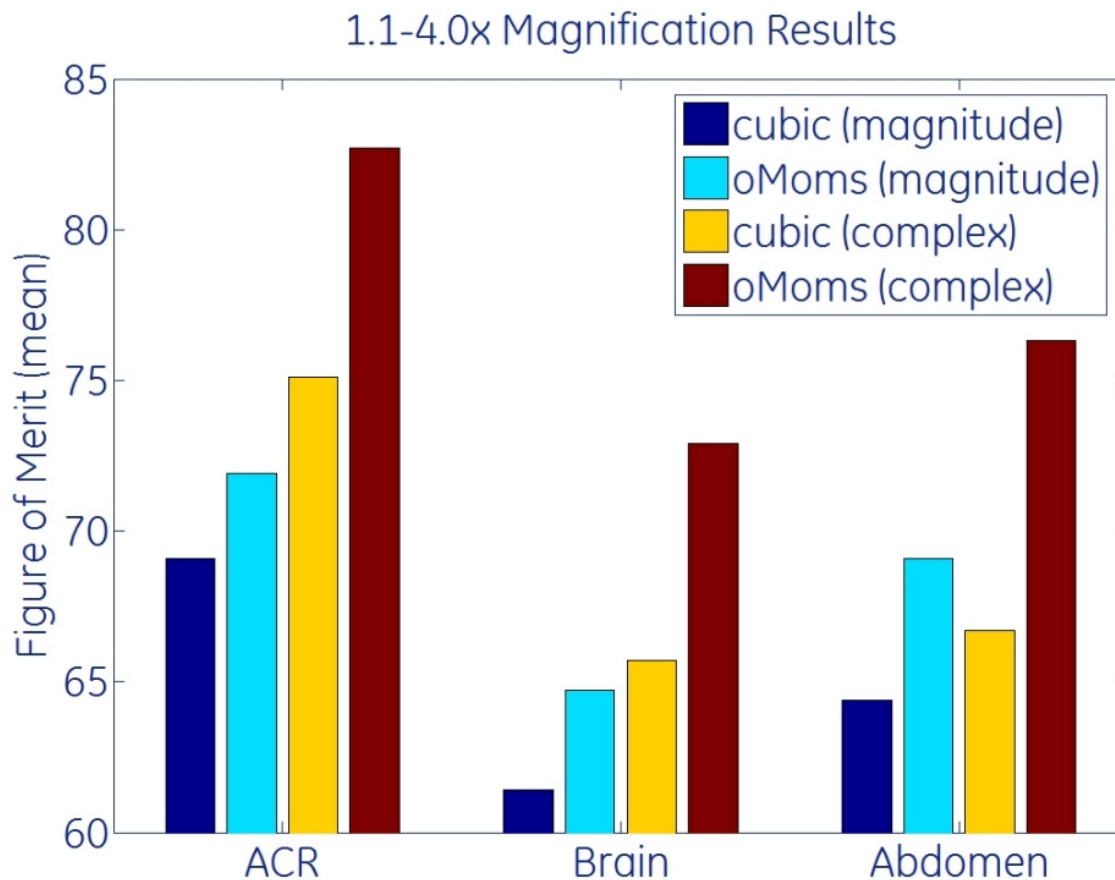


Figure 22. Likeness of interpolation schemes to complex sinc.

For the ACR phantom, brain and abdomen data sets there was a quantitative improvement in approximation when moving from either magnitude to complex data or from cubic interpolation to cubic oMOMS generalized interpolation. When comparing the combined employment of both strategies versus neither, a 20% mean improvement to this metric was seen across all data sets. Qualitative image analysis is given in the next section.

3.3.1 Phantom Results

The experiment with the ACR phantom is explored first in the left column of Figure 23. The original image shows the entire slice chosen for the feature of having resolution holes, which range from 1.1mm on the left, 1.0mm in the center and 0.9mm on the right. As described in [20], the resolution holes are intentionally staggered along the x and y axis for the purpose of the accreditation tests not being impacted by partial volume artifacts. Displayed next is a portion of the phantom resulting from a 3.0x magnification followed by taking the absolute difference between the reference complex sinc interpolation and the cubic interpolation of magnitude data (Figure 23b - Left) as well as the difference with the cubic oMOMS interpolation of complex data (Figure 23c - Left). The same window-level was used for the difference images, and it is apparent that the first technique struggles to retain edge information. Lastly, the resolution holes are also displayed after 3.0x magnification for the complex sinc (Figure 23d - Left), cubic interpolation of magnitude data (Figure 23e - Left), and o-MOMS interpolation of complex data (Figure 23f - Left). In addition to the resolution holes between easier to distinguish from the complex generalized interpolant (f) than cubic convolution (e), an interesting feature easily seen from the center 1.0mm holes is that (e) has incorrectly positioned the rows and columns as running straight along the axis. They are no longer staggered as expected from the physical phantom and as shown in both (d) and (f). Using complex data along with generalized interpolation improved the likeness to results from a complex sinc-interpolation and to what we expect from the scanned object.

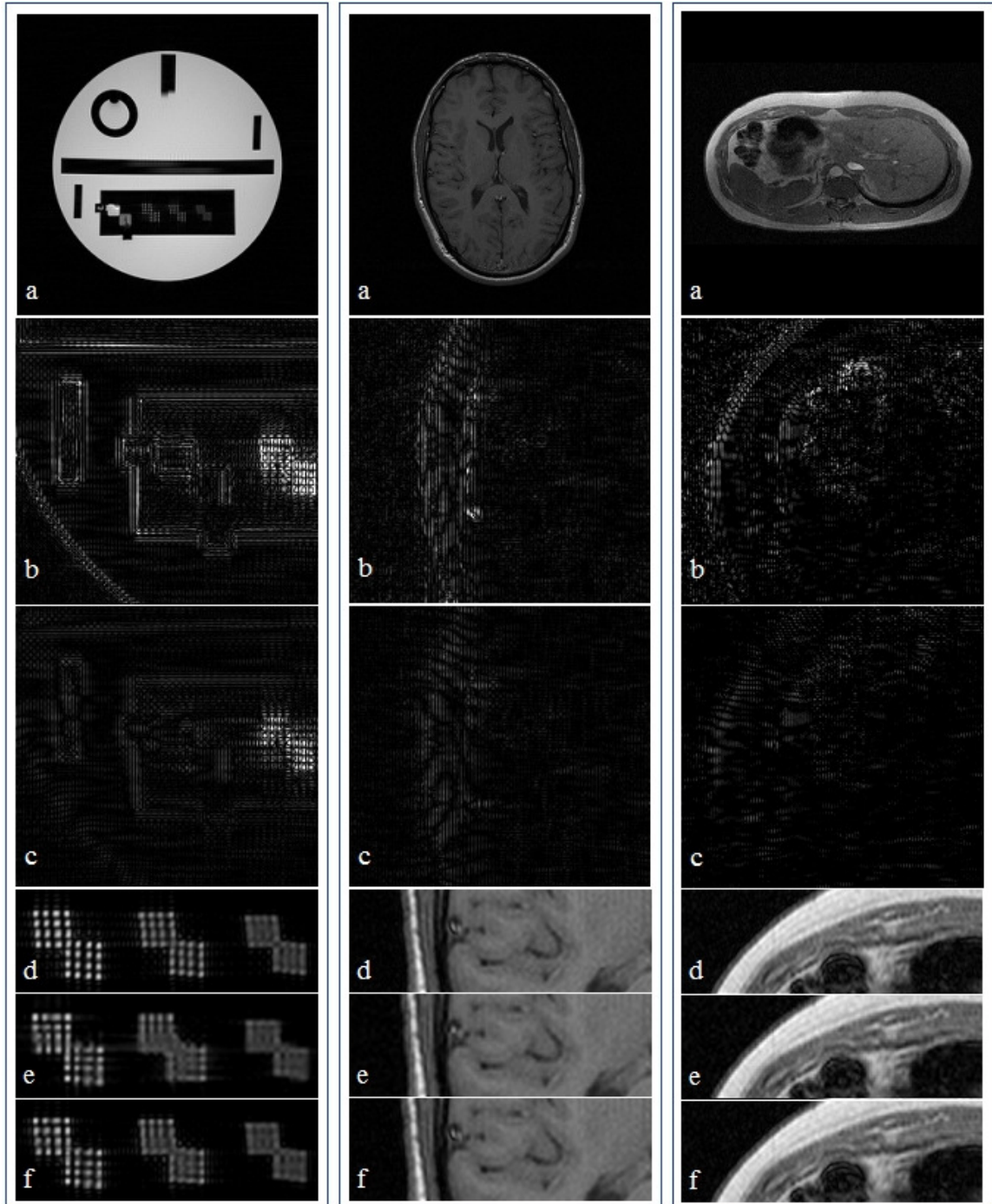


Figure 23. Left: ACR Phantom. Center: Brain. Right: Abdomen. For all figures: (a) Original image. Difference between complex sinc 3.0x magnification compared to (b) magnitude cubic, (c) complex oMOMS. Image after 3.0x zoom of (d) sinc, (e) magnitude cubic and (f) complex oMOMS.

3.3.2 *In-vivo Results*

The original T1-weighted brain image (Figure 23a - Center) and similar magnified images to the prior phantom analysis are shown. The higher-order interpolant working on complex data shows less difference with the reference. Using the brightest region of the difference image (b) as a guide, there is a blood vessel running through the axial slice that can be seen to have lost the dark surrounding boundary between it and the neighboring tissue.

Analysis of the multi-coil abdomen data shows the same pattern of the conventional technique struggling with sharp boundaries made up of higher frequency information. The difference image (b) can be used as a guide to focus on the curved edge bordering the abdominal muscle with intestine. The sinc and complex oMOMS interpolated images do not show the muscle protruding slightly into the intestine as the cubic does.

3.4. *Discussion and Conclusion*

Across all data sets, cubic interpolation of magnitude data (Figure 23e) tended to blur fine structures while the utilization of phase information and a higher order estimate as in (Figure 23f) preserves details. The single channel neuro and multi channel abdominal in-vivo data have shown consistent behavior with the phantom results in quantitative measurement as well as qualitative image inspection.

Improved magnification of MR images has been demonstrated through higher order interpolation of complex data. While applied in two dimensions for this analysis,

the separable interpolation can be used for any number of dimensions of data being magnified.

4. Application to MR Gradient Non-linearity Correction

4.1. Introduction

This chapter will look at extending the generalized interpolation results to the application of distortion correction due to gradient non-linearity. The nonlinearity of the gradients causes the distortion from the physical magnet coordinate system (x_p, y_p, z_p) to the warped coordinate system (x_w, y_w, z_w) . Higher order polynomials, in this case 5th order, are used to represent the mapping from physical to warped space. The polynomial coefficients making up the equations describing the mapping can be determined from the spherical harmonic expansion of the magnetic field. Spatial distortion is then corrected by deriving the gradient error from this mapping [1] in order to map the warped object back to physical space. Since this mapping rarely falls on pixel boundaries, this correction is conventionally performed by computing each physical pixel from an interpolated neighborhood of the warped image. For the modest gradient errors found in standard imaging, where axis error correlation is insignificant, this interpolation can be performed separably. For example, a two dimensional image would have the x-direction correction performed in one stage of processing and the y-direction correction performed in a separate stage. As more nonlinear gradient coils are used, such as local planar gradients [21], a non-separable interpolation may be needed for accuracy. The use of MR for abdominal imaging over neuro imaging also increases the effective nonlinearity of the image. This is due to the distortion increasing away from the center of the magnet, or isocenter, along with the larger field of view including this distortion in the image, which causes the separable approximation to no longer hold.

4.2. Methods

The prior chapter examining MR image magnification showed both a qualitative and quantitative assessment that higher order interpolation can provide a better approximation. Beyond visual inspection a metric was computed to see how close an image was to an expected result. This was straightforward in the case of magnification, but for distortion correction we do not have a known, undistorted reference for comparison. The only known reference is the distorted image itself, so a method for using this to our advantage is created.

4.2.1. Separability

In the earlier rotation and magnification experiments, two separable 1D interpolation steps could be performed without concern for position accuracy due to the rigid-body nature of the transformation. The tradeoff in computation time for an N -point interpolant scales by $2N$ rather than N^2 , for separable and non-separable 2D transformations respectively, so the choice is straightforward for these rigid-body transformations. For gradient nonlinearity correction however, the image is deformed in such a way that this separable assumption is no longer strictly valid. Practically, when using a separable kernel, as the amount of pixel displacement becomes larger (i.e.- further away from isocenter) the inaccuracy of the pixel positions becomes more noticeable.

A one-dimensional function, such as the Keys cubic, can be extended to a two-dimensional function as the multiplication of two one-dimensional functions. Extending the generalized interpolation framework to a non-separable implementation is not as straightforward. Since the prefilter stage does not actually displace any pixels, we apply

this stage to the two-dimensional image first along the rows and then along the columns of the image. The one-dimensional o-MOMS interpolant function (1.17) is then extended to two dimensions in the same way the Keys cubic was. The image that has been pre-filtered in all dimensions is input to the non-separable distortion correction. This hybrid approach of having a separable pre-filter and non-separable distortion correction allows for the fast pre-treatment of the data along with an accurate correction. This can be extended to any number of dimensions, although it will only be applied to a two-dimensional image here.

4.2.2. Forward-Inverse Distortion Correction

The method for mapping warped space to physical space is straightforward from the implementation perspective, as described above. In order to perform the inverse operation, however, one needs some way of mapping backwards. Analytically inverting the fifth-order polynomial in three dimensions would be ideal, but has the drawback of being not only computationally intensive, but also being specific to each gradient coil design. Solving the problem from a computational optimization approach from [10] can take considerable time, on the order of hours in MATLAB (The Mathworks, Natick, MA), and is specific to a single acquired slice orientation within a gradient coil. The procedure used here for computing the inverse mapping from physical space to warped space is to store into memory the pixel-to-pixel error mapping for each axis from the forward, warped to physical correction, and individually map each of these backwards. This works under the assumption that gradient error surrounding an individual pixel changes slowly and can be approximated by simple linear interpolation. This has the

advantage of taking less than a second to compute and can be used in-line for use with any gradient coil and slice orientation. Also, corrections for pixel intensity due to voxel size distortion will be disabled for the forward-inverse correction experiments to show effects from interpolation only with no impact from this spatially varying intensity correction.

4.2.3. Error Measurement

The figure of merit used earlier (1.15) for comparing an approximated image ($g_{x,y}$) to a reference image ($f_{x,y}$) made comparing across data sets difficult. There is a lack of normalization based on overall signal values and no parameter to account for error imposed from a multiple number of transformations. For this forward-backward distortion correction, we propose using a metric based on root-mean squared error (RMSE) measurement with two modifications in order to quantify the amount of error imposed during normal distortion correction. The first is that it will be divided by the mean of the approximated image to provide overall image magnitude normalization, and the second is that this normalized RMSE will be divided by two as the measured error has been the result of to two transformations,

$$GW_RMSE = \frac{\sqrt{\sum_{x,y=1}^{len_{x,y}} (f_{x,y} - g_{x,y})^2}}{2 \sum_{x,y=1}^{len_{x,y}} |f_{x,y}|}. \quad (1.18)$$

With this equation, a perfect approximation where $f_{x,y} = g_{x,y}$ will result in a $GW_RMSE=0.0$. As a part of standard forward transformation, a small percentage of pixels in the image can be subject to being moved completely off of an image, so are

discarded as part of the correction. Attempting to map pixels from outside the image boundaries into the image during the inverse correction will result in a pixel value of zero. In order for the difference between the original value that resided at that point being compared to zero to not improperly skew the measurement, these pixels are not considered in the GW_RMSE measurement.

4.2.4. Data Collection

We implement the above experiments on raw k-space data acquired from a 3.0 Tesla Signa HDx MRI scanner (GE Healthcare, Waukesha, WI) with a whole body gradient system (slew rate = 200 Tesla/m/s, max amplitude 5 Gauss/cm) and an 8-channel HD torso array coil was. The pulse sequence used for the coronal acquisition was a 3D dual-echo spoiled gradient echo, which is designed so that water and fat are out-of-phase for the first echo ($TE_1=1.2\text{ms}$) and in-phase for the second echo ($TE_2=2.4\text{ms}$), and each are collected after just one RF excitation ($TR=4.1\text{ms}$) with flip angle of 12 degrees. The acquired matrix is $320 \times 192 \times 44$ with a 48cm field of view (FOV), slice thickness of 4.0mm and receiver bandwidth (RBW) of $\pm 167\text{kHz}$. Parallel imaging was not used for this 28 second acquisition and the coil combination was a sum-of-squares reconstruction to a matrix size of $320 \times 320 \times 88$. This acquisition was intentionally chosen to test the techniques on one data set with many sharp edges where fat and water border one another causing cancellation (Figure 24 - Left), and a second data set that has much less high frequency content (Figure 24 - Right). The two data sets are perfectly registered despite the different contrasts, so clinically this pulse sequence plays an especially useful role in cases of fatty infiltration of the liver.

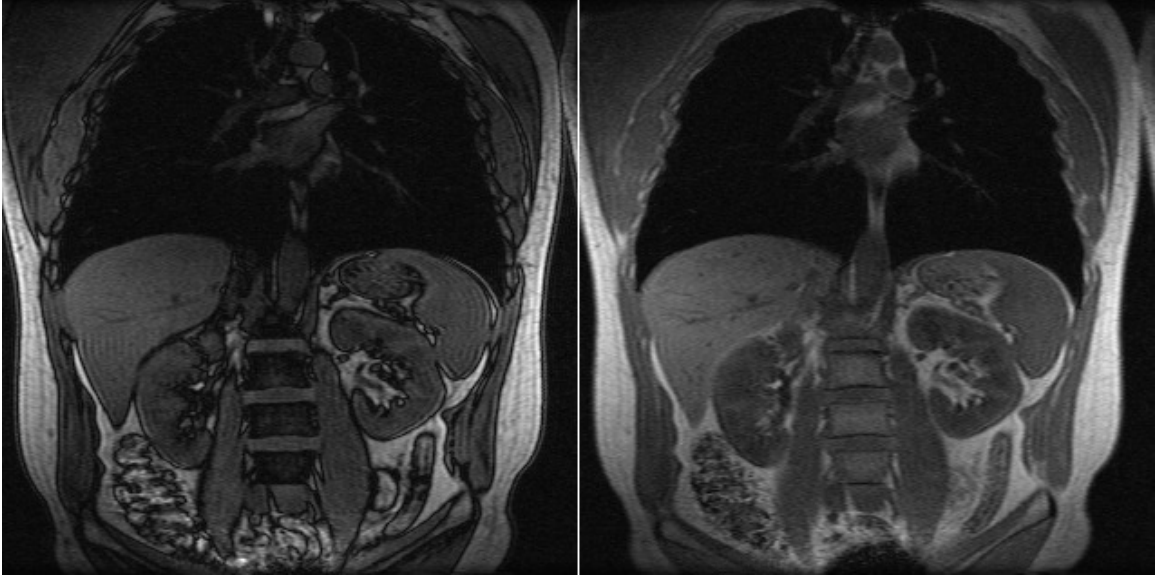


Figure 24. Left: Acquired out-of-phase. Right: Acquired in-phase.

4.3. Results

Using the out-of-phase (OOP) image as a beginning for comparison, (Figure 25 - Left) shows the result of using a separable Keys cubic interpolation (1.16), the fastest overall method considered here. The hybrid non-separable application of cubic oMOMS is shown in (Figure 25 - Right). Looking to the extremities of the FOV, such as the hips and shoulders, one can see the overcorrection due to error from the first evaluated axis impacting the interpolation of the following.

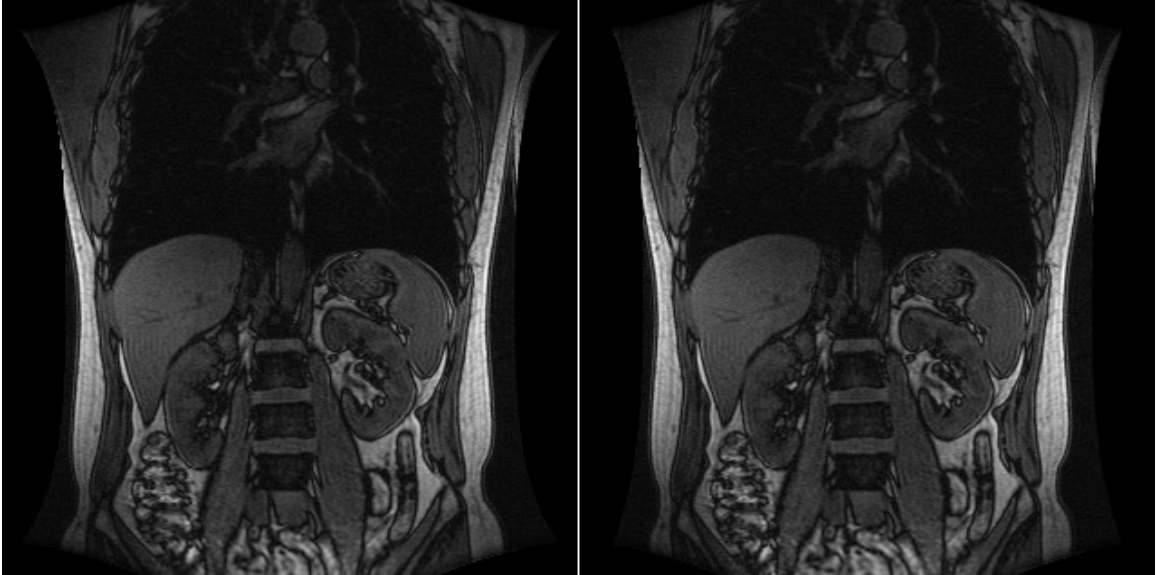


Figure 25. Left: Separable distortion correction applied to OOP. Right: Nonseparable correction.

To help visualize the effects of the faster separable interpolation scheme on in-vivo data, the out-of-phase (OOP) data was corrected with each 1D and 2D correction techniques. Medical images are generally viewed as a grayscale colormap. The results of separable 1D correction is converted to a purely red image while the 2D correction is Blue-Green (Figure 26), so that the color vectors are pointing in opposite directions. The two RGB images are then averaged giving a result which is purely grayscale in regions where there is no separability error and color biased where differences in image contrasts occur (Figure 27 - Left). To more easily see differences in low signal regions, the color vector directions are maintained while the magnitude is maximized so the pure white pixels represent no error from the separability assumption (Figure 27 – Right). From this view it shows that the separability assumption is valid for the central portion of the image, but at the extremities there is noticeable error.

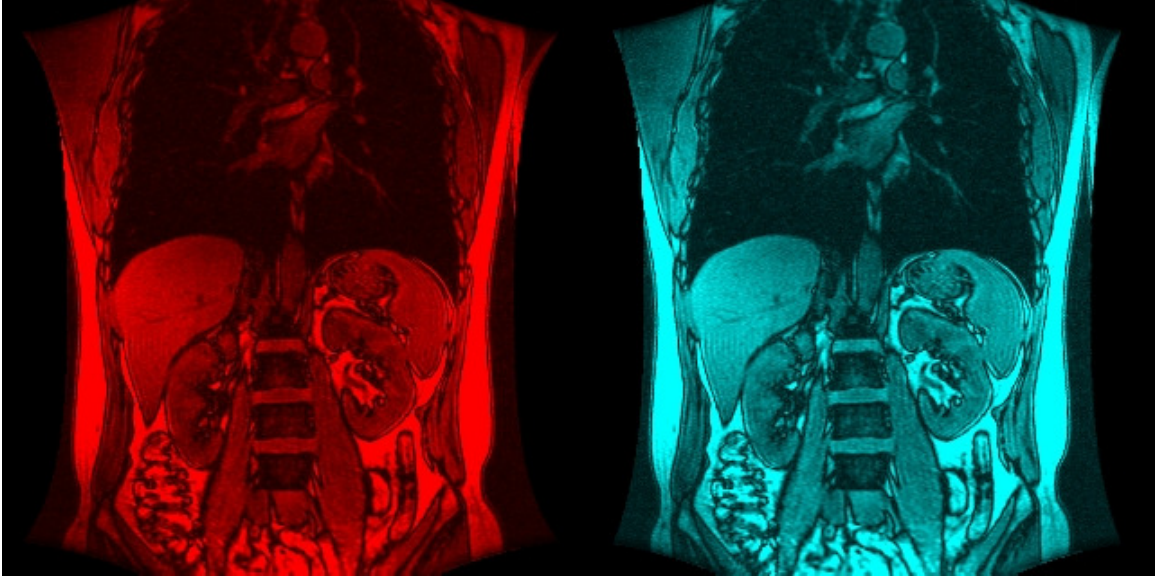


Figure 26. Left: Nonseparable results in Red, Right: Separable results in Green-Blue.

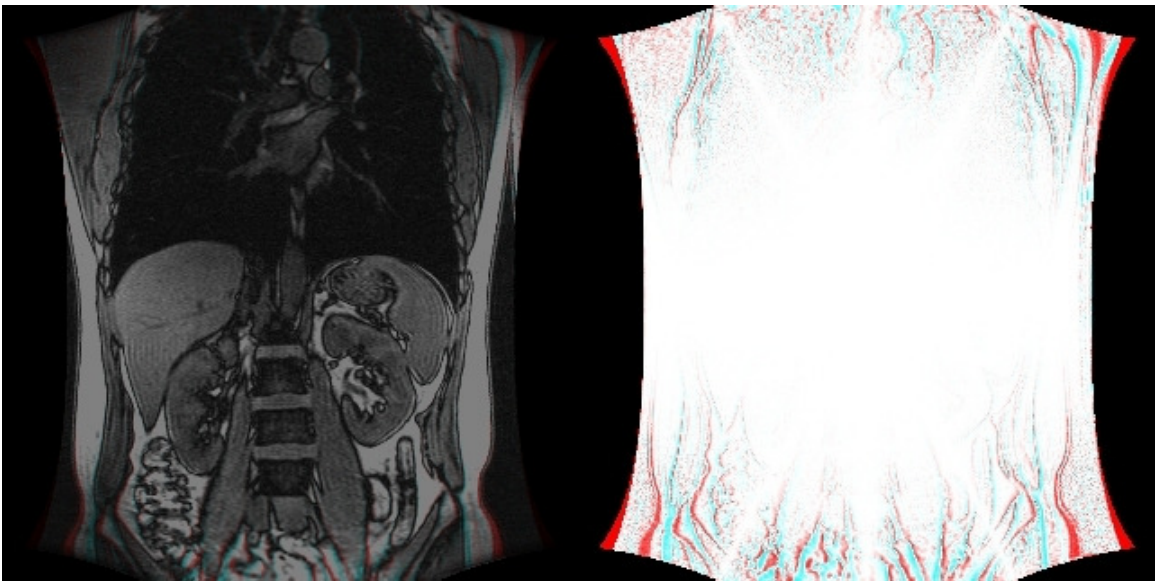


Figure 27. Left: Color Difference between separable (R) and nonseparable (GB) correction. Right: Maximized color vectors of same image.

The GW-RMSE measurement was evaluated separately for each slice and each echo of the coronal abdomen data set. Plotted results are shown in Figure 28 and show

that for this data, the higher order interpolant and non-separable distortion correction scheme each lower the error compared to the reference.

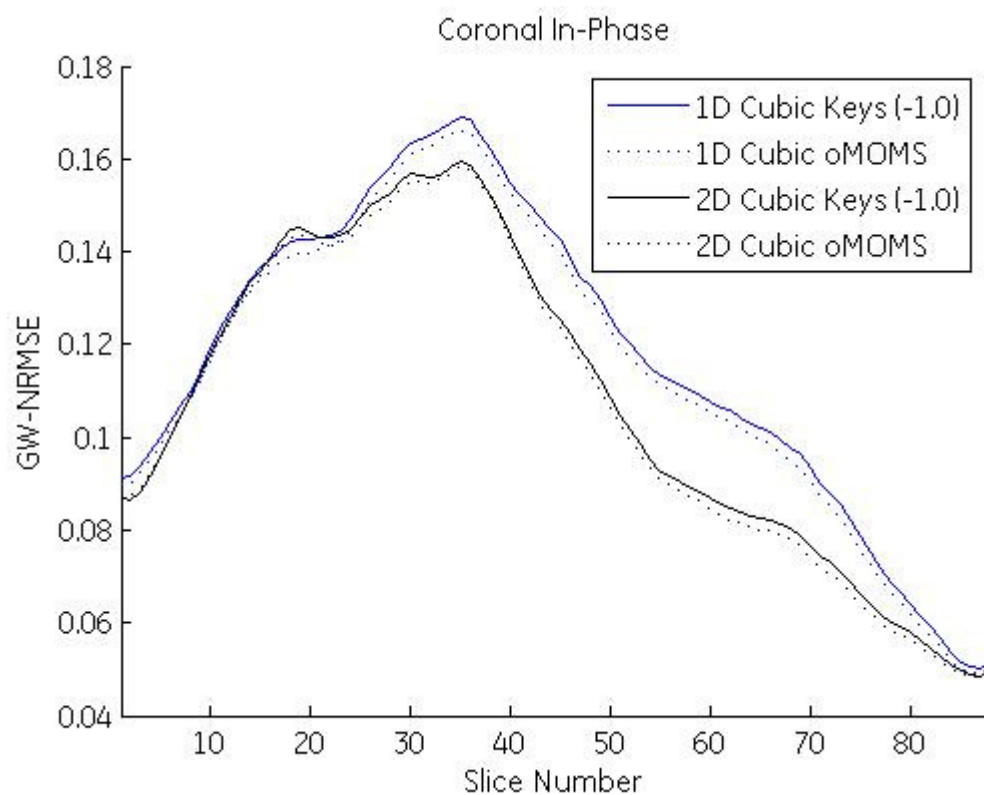


Figure 28. Mean-normalized root mean square error per slice location of in-phase data.

Table 1 shows the mean and standard deviation across the slices for the error measurement. The non-separable transform showed to have the most impact on reducing error, improving the mean by 8.6%. The generalized interpolation scheme also showed improved performance, but by only 1.7% overall. The overall error improvement from the combination of the two techniques is 10%. Next, visual comparisons of these two cases are shown.

Table 1: Mean and standard deviation of GW-NRMSE In-phase data results for different separability and interpolation types.

Input	Separability	Interp Type	Mean GW-NRMSE (stdev)
IP	1D	Cubic Keys (-1.0)	0.11703 (0.03380)
IP	1D	Cubic oMOMS	0.11459 (0.03353)
IP	2D	Cubic Keys (-1.0)	0.10734 (0.03483)
IP	2D	Cubic oMOMS	0.10591 (0.03483)

Shown below (Figure 29) are resulting images from the forward-inverse gradient distortion correction for the separable cubic Keys interpolation, along with the absolute difference with the original. Similar to what was shown with the color vector experiment, there is little issue in the center of the image where the distortion is very low. The corners of the image show the majority of displacement error. Figure 30 shows similar characteristics, but with less displacement error. While this image doesn't have many sharp edges, the border between the lung and chest wall looks to have reduced differences.

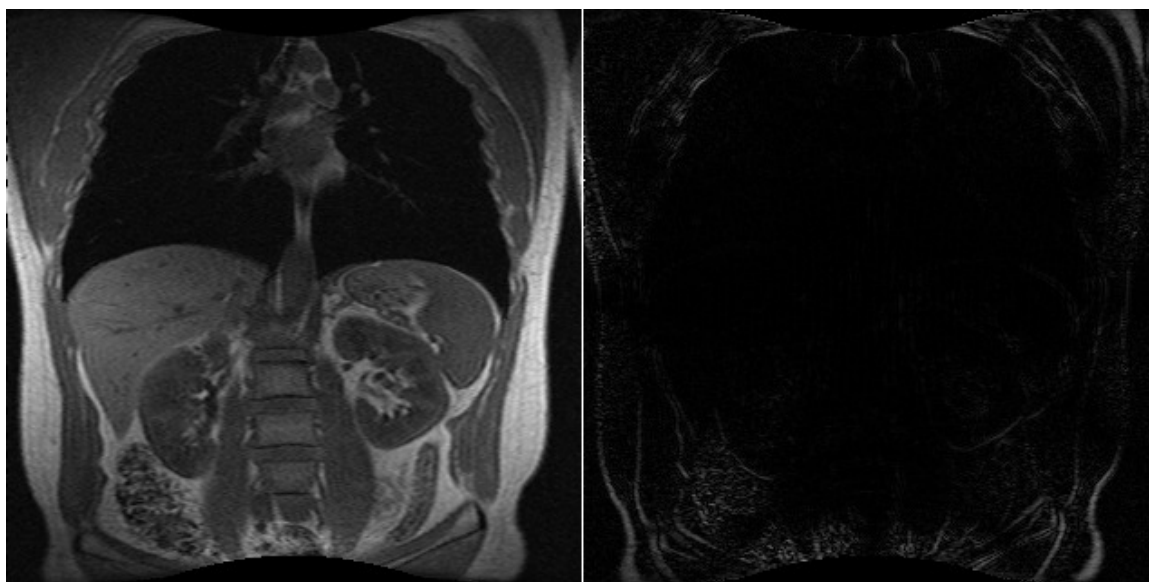


Figure 29. Left: Forward-Inverse correction of IP with separable cubic Keys (-1.0). Right: Difference with Original

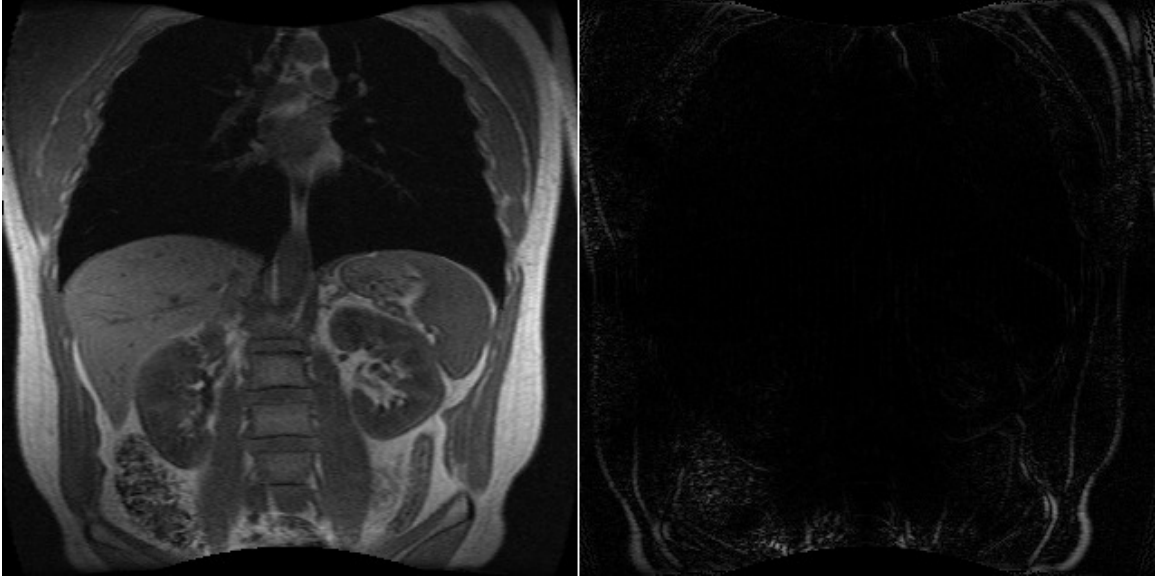


Figure 30. Left: Forward-Inverse correction of IP with nonseparable cubic oMOMS. Right: Difference with Original

For the out-of-phase data with higher sharp edge content, the GW-RMSE measurement was again evaluated separately for each slice of the coronal abdomen data. Plotted results are shown in Figure 31 and show that for this data the overall error across all techniques is higher than from the in-phase data. As before, for the majority of the slices the non-separable distortion correction scheme lowered the error compared to the reference. For all slices, the higher order interpolation showed better performance.

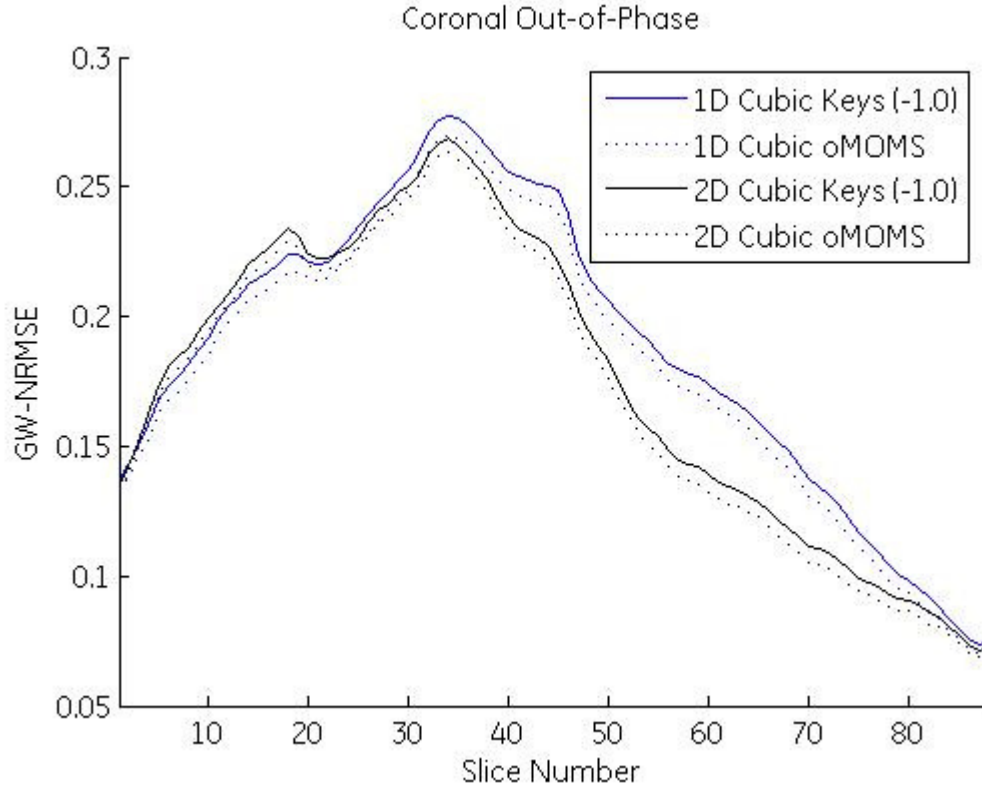


Figure 31. Mean-normalized root mean square error per slice location of out-of-phase data.

Table 2 shows the mean and standard deviation of the error has increased by approximately 1.7x over the in-phase data, the same techniques gives less error in both cases. The improvement from non-separable correction is 6.7% overall for this OOP data, and the oMOMS interpolation type improved the correction by 3.2%. Comparing the best performing to the worst performing overall, is a 10% difference in this metric.

Table 2 Mean and standard deviation of GW-NRMSE Out-of-phase data results for different separability and interpolation types

Input	Separability	Interp Type	Mean GW-NRMSE (stdev)
OOP	1D	Cubic Keys (-1.0)	0.18706 (0.05741)
OOP	1D	Cubic oMOMS	0.18077 (0.05664)
OOP	2D	Cubic Keys (-1.0)	0.17482 (0.05982)
OOP	2D	Cubic oMOMS	0.16978 (0.05975)

Shown below (Figure 32) are resulting image from the forward-inverse correction for the separable cubic Keys interpolation, along with the absolute difference with the original. This OOP data has more edge information and just as the image error calculation predicts, there are more differences along the fat-water boundaries. The corners of the image show the majority of error, but more subtle differences are seen in the center of the differences in comparison to the IP data. Figure 33 has a similar behavior, and like the IP comparison, the boarder between the lung and chest wall looks to have reduced differences.

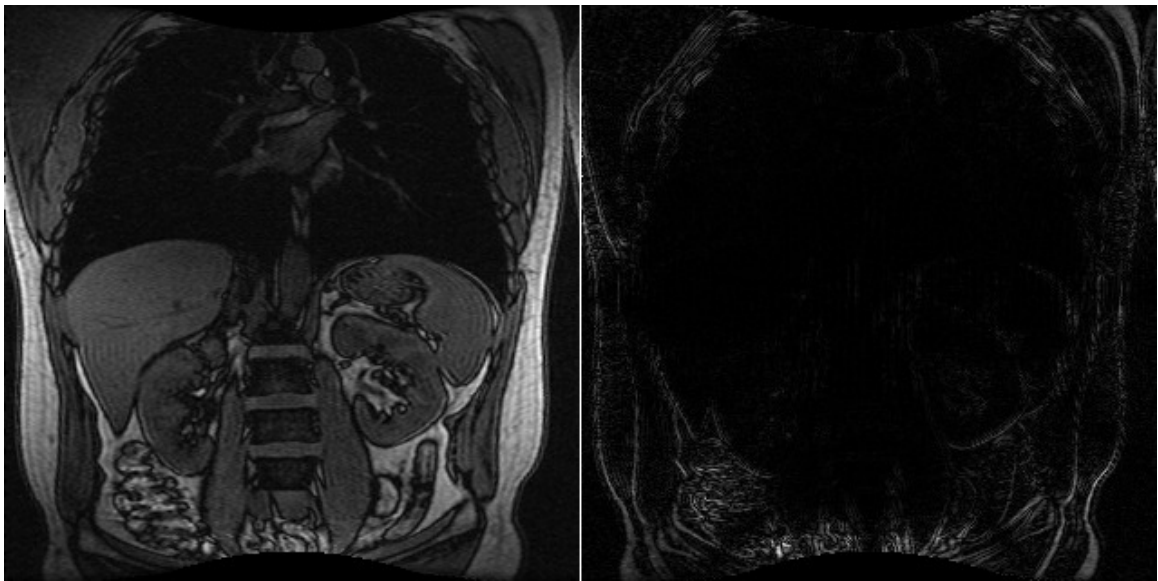


Figure 32. Left: Forward-Inverse correction of OOP with separable cubic Keys (-1.0). Right: Difference with Original

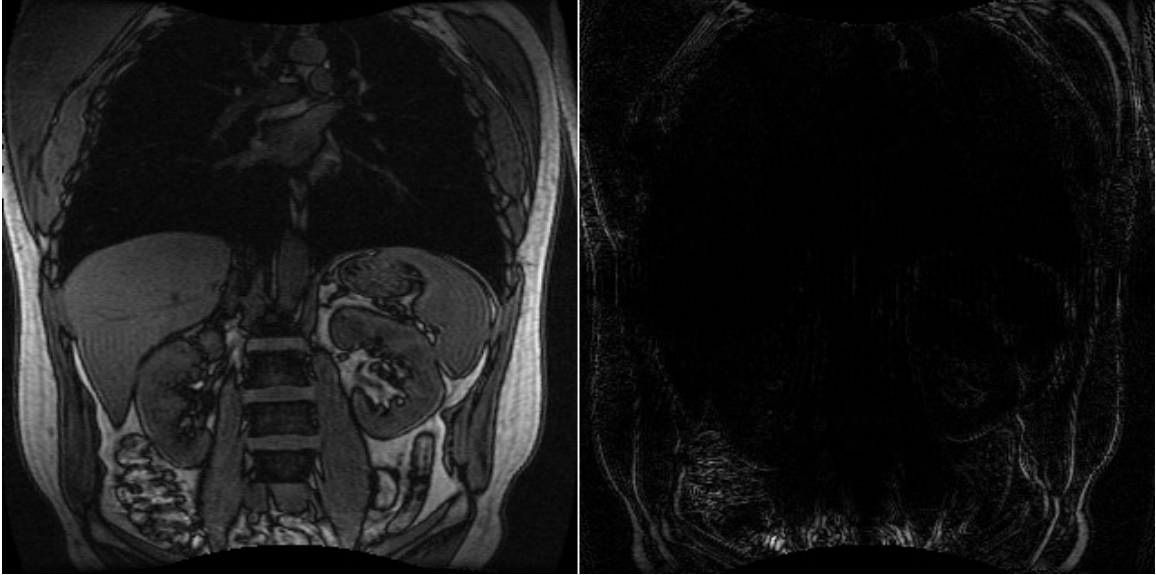


Figure 33. Left: Forward-Inverse correction of IP with nonseparable cubic oMOMS. Right: Difference with Original

4.4 Discussion and Conclusion

The improvement from cubic Keys to cubic oMOMS for separable and non-separable schemes demonstrates the hybrid approach of this non-separable oMOMS prefilter and interpolant scheme is a reasonable extension of the strictly one dimensional technique applied in prior work.

With these experiments above, the forward-inverse gradient distortion correction and RMSE measurement comparing approximated results against the original images gives a quantitative metric for comparing error between different data sets as well as between different interpolation techniques. The overall error increased, as expected, when moving from the in-phase data to the out-of-phase data from the same acquisition.

While the quantitative differences supported the hypothesis that higher order interpolation would give improvement, the qualitative inspection of images didn't show as significant an improvement as with the prior image analysis of magnification images.

This is due to the fact that for a 3.0x zoom example, every neighborhood of nine pixels only has one original and eight approximates. This gradient distortion correction case looks like a less problematic application in the way we implemented it here, in that a large portion of the image has little displacement error. The higher order interpolation scheme would have more impact if the processing step of gradient non-linearity correction were extended to have a larger need for upsampling. Potential applications could be the removal of the zero-padded reconstruction step, which upsamples the images before performing gradient distortion correction, in favor of using the correction itself to magnify images.

5. Summary

5.1. Discussion & Conclusion

In Chapters Two, Three and Four, the applicability of generalized interpolation as a higher quality approximation over the cubic convolution kernel has been demonstrated at a relatively inexpensive cost. Chapter Two demonstrates the four-point cubic oMOMS technique to perform near or better than a 16-point apodized sinc for the simulated phantom tasks. For the task of magnification, we couple this interpolant with the use of complex MR data to demonstrate through quantitative measurement and qualitative image inspection of phantom and in-vivo data that the image quality exceeds the status quo of using a cubic interpolation for image manipulation. Furthermore, the cost of the extra prefiltering step is shown to approach zero as the amount of magnification is performed. Chapter 4 looks at the special case of gradient non-linearity correction, a non-rigid transformation which can demand a non-separable mapping from warped to physical space. We extend the generalized interpolation scheme, only used in a separable implementation in all referenced work and prior chapters, to a hybrid non-separable framework. The prefiltering is performed separably and the mapping stage is done non-separably. The quantitative measurements made on forward-inverse distortion correction show that the technique decreases the amount of error incurred over a standard cubic kernel for both separable and non-separable corrections.

5.2. Future Work

This thesis demonstrates three improvements that can be made to an MR image by leveraging higher order interpolants, complex data, and non-separable interpolation.

Let us consider an acquired slice from Chapter 4, where a 320x192, 8 channel acquisition is zero-interpolated to be reconstructed via sum-of-squares to a final image size of 512x512 as shown in Figure 34.

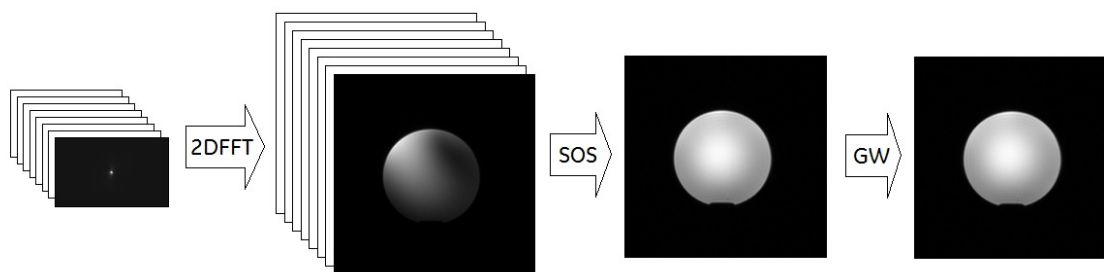


Figure 34. Recon processing where k-space is zero-padded first and distortion correction is done on the magnitude sum-of-squares (SOS) image.

Using the cubic o-MOMS interpolant to perform a non-separable, complex interpolation instead of a cubic Keys with separable interpolation of magnitude data makes correcting for gradient non-linearity become 112 times slower. The majority of this extra time is due to the complex coil information being lost in the sum-of-squares, forcing the distortion correction to be done for all eight channels separately, as shown in (Figure 35).

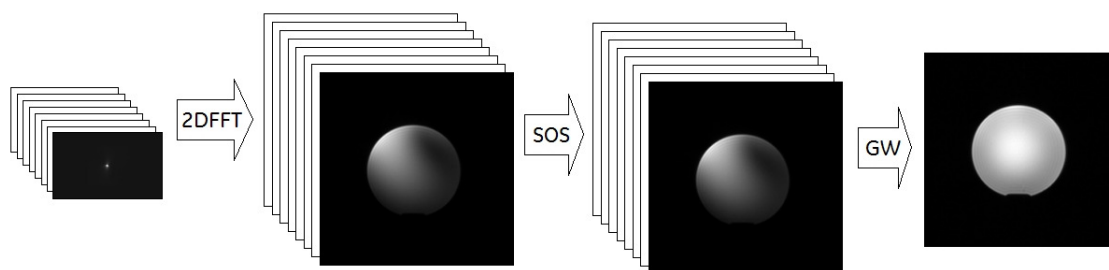


Figure 35. Recon processing where gradient distortion correction must be performed on each individual coil to have access to complex data.

Other techniques, such as SENSE [22], can be used for phase sensitive coil combination, but were not considered in the scope of this thesis due to their own image quality and computation considerations. These methods are often used anyway as part of the parallel imaging unaliasing, and this complex combination removes the coil-by-coil distortion correction penalty down from 112 to 14 times slower for this example. The next step to speed up the impact of these new techniques would be to investigate a separable correction scheme which takes into consideration the location error it imposes, and compensates to be as accurate as the non-separable method. This would then lower the computational impact of the more accurate distortion correction scheme from 14 down to 3.5 times. Furthermore, given the close likeness of the generalized interpolant to a sinc function in Chapter 3, one could consider doing acquired size FFT of each channel, with implementations that can scale non-powers-of-2 by $n \log_2 n$ [23], would reduce 512x512 to 320x192 by approximately 5 times, as shown in Figure 36.

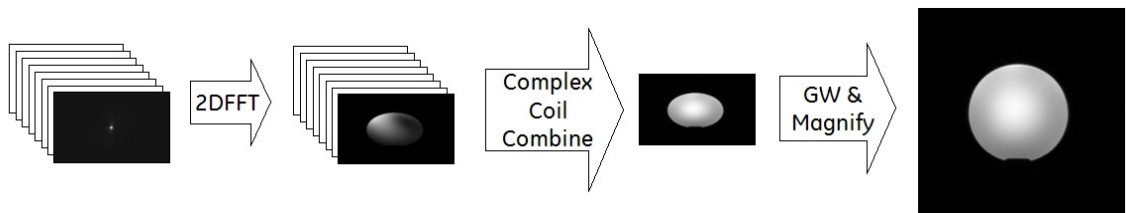


Figure 36. Complex coil combination allows for more acquired size processing and use of higher order, complex magnification within the gradient distortion correction step.

This will lower the reconstruction and coil combination time. Furthermore, the approach imposed to perform generalized interpolation non-separably by pre-filtering all dimensions first could be applied back to the magnification section where the prefilter

computation overhead improved by magnification factor, but not by dimensionality. One could leverage this and still use the separable interpolation strategy and begin to see less overhead as dimensionality increased (Figure 37).

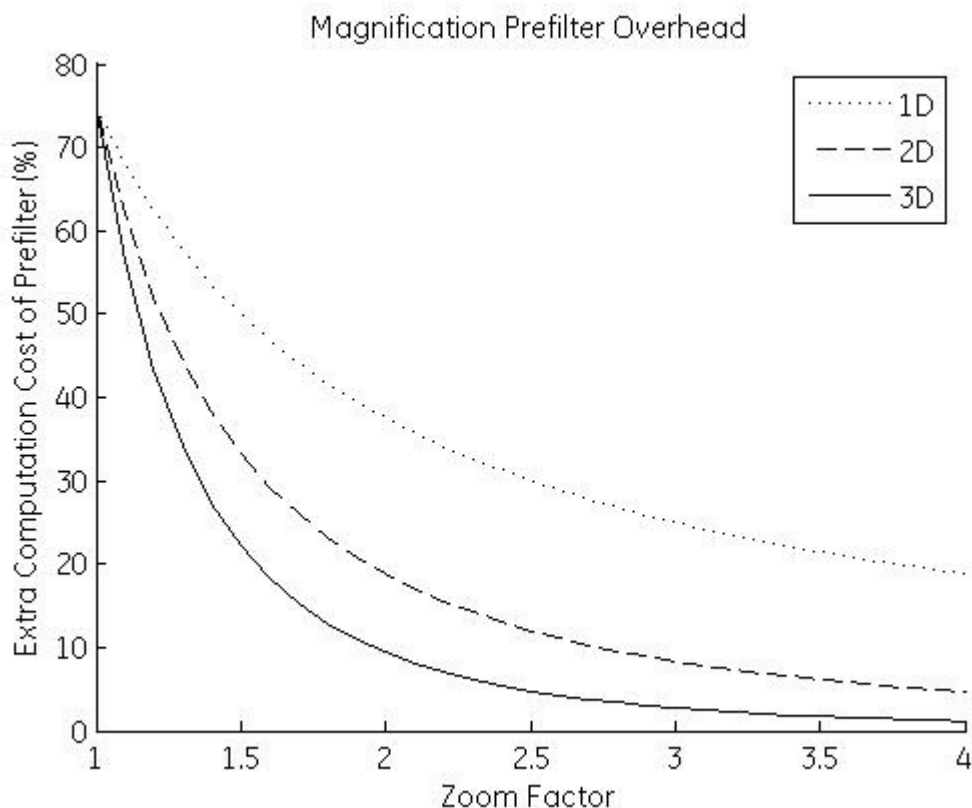


Figure 37. Additional cost of the prefiltering stage over cubic interpolation.

This could allow for the prefilter overhead to diminish to the point where the only overhead from gradient distortion correction is from considering complex data. This two-times penalty has potential to be worthwhile, not only for the improved image quality, but also for making the computation and storage cost of the reconstruction chain to be less expensive when distortion correction and magnification can be performed in one step.

Another application to extend this to would be aspect ratio maintenance for rectangular field-of-view acquisitions. For example, today a 320x192 acquisition can be prescribed to cover 44 cm in one direction and 38 cm in another. Today, this would be reconstructed up to a 512x512 matrix and downsampled during gradient distortion correction to cover 512x442 image pixels maintaining the acquired aspect ratio. Similar to the multi-coil combination block diagrams above, one could consider a small, acquired size reconstruction followed by a gradient distortion correction that upsamples to get the same size output image but with a reconstruction made up of less operations.

6. References

1. Glover G, Pelc NJ. Method for Correcting Image Distortion Due to Gradient Nonuniformity. US Patent 4,591,789; 1986.
2. Keys R. Cubic convolution interpolation for digital image processing. IEEE Transactions on Acoustics, Speech, and Signal Processing 1981;29(6):1153-1160.
3. Blu T, Thevenaz P, Unser M. Minimum support interpolators with optimum approximation properties. IEEE International Conference on Image Processing 1998:242-245.
4. Blu T, Thevenaz P, Unser M. MOMS: Maximal-order interpolation of minimal support. IEEE Transactions on Image Processing 2001;10(7):1069-1080.
5. Thevenaz P, Blu T, Unser M. Interpolation revisited. IEEE Transactions on Medical Imaging 2000;19(7):739-758.
6. Nishimura DG. Principles of Magnetic Resonance Imaging; 1996.
7. Bernstein MA. Method for correcting MR phase information image data. US Patent 5,642,047; 1997.
8. Polzin JA, Kruger DG, Gurr DH, Brittain JH, Riederer SJ. Correction for gradient nonlinearity in continuously moving table MR imaging. Magnetic Resonance in Medicine 2004;52(1):181-187.
9. Kruger DG, Polzin JA. Self Correcting Transform for Non-linear Magnetic Field Gradients in MRI. Proceedings of the 11th Annual Meeting of ISMRM, Toronto, Canada 2003.

10. Slavens ZW, Polzin JA, Ward HA. Real-time Gradient Non-linearity correction. Proceedings of the 12th Annual Meeting of ISMRM, Kyoto, Japan 2004.
11. Parker JA, Kenyon RV, Troxel DE. Comparison of Interpolation Methods for Image Resampling. IEEE Transactions on Medical Imaging 1983;MI-2(1):31-39.
12. Unser M, Fellow L. B-Spline Signal Processing: Part I-Theory. IEEE Transactions on Signal Processing 1993;41(2).
13. Unser M, Aldroubi A, Eden M. B-spline signal processing. II: Efficient design and applications. IEEE Transactions on Signal Processing 1993;41(2):834-848.
14. Harris FJ. On the use of windows for harmonic analysis with the discrete Fourier transform. Proceedings of the IEEE 1978;66(1):51-83.
15. Oppenheim AV, Schafer RW. Discrete-time signal processing: Prentice-Hall, Inc. Upper Saddle River, NJ, USA; 1989.
16. Tong R, Cox RW. Rotation of NMR images using the 2D chirp-z transform. Magnetic Resonance in Medicine 1999;41(2):253-256.
17. Slavens ZW, Hinks RS, Polzin JA, Johnson MT. Improved MR Image Magnification by Generalized Interpolation of Complex Data. Proceedings of the 15th Annual Meeting of ISMRM, Berlin, Germany, (Abstract #1887) 2007.
18. Smith MR, Nichols ST. Efficient algorithms for generating interpolated (zoomed) MR images. Magnetic Resonance in Medicine 1988;7(2):156-171.

19. Ahn CB, Cho ZH. A new phase correction method in NMR imaging based on autocorrelation and histogram analysis. *IEEE Transactions on Medical Imaging* 1987;6(1):32-36.
20. Phantom Test Guidance for the ACR MRI Accreditation Program. Reston, VA: American College of Radiology; 1998.
21. Aksel B, Marinelli L, Collick BD, Von Morze C, Bottomley PA, Hardy CJ. Local planar gradients with order-of-magnitude strength and speed advantage. *Magnetic Resonance in Medicine* 2007;58(1):134-143.
22. Pruessmann KP, Weiger M, Scheidegger MB, Boesiger P. SENSE: sensitivity encoding for fast MRI. *Magnetic Resonance in Medicine* 1999;42(5):952-962.
23. Frigo M, Johnson SG. The Design and Implementation of FFTW3. *Proceedings of the IEEE* 2005;93(2):216-231.

7. Appendix

Proceedings of the 15th Annual Meeting of ISMRM, Berlin, Germany 2007 (Abstract #1887)

Improved MR Image Magnification by Generalized Interpolation of Complex Data

Z. W. Slavens^{1,2}, R. S. Hinks¹, J. A. Polzin¹, and M. T. Johnson²

¹GE Healthcare, Waukesha, WI, United States, ²Marquette University, Milwaukee, WI, United States

Introduction

Image viewing and manipulation is common on MR scanners and workstations as a convenient means of magnifying, rotating, and shifting of the data for closer inspection. When an image is pulled out of a database and interaction with this data requires information to be made available off of the Cartesian grid, interpolation is used to determine the missing information. A cubic interpolation kernel is often used because it does not suffer from the same artifacts that can be caused by nearest neighbor or linear interpolation, while still being small enough in size to be computationally reasonable. This limited kernel support can still have a low-pass effect on the image however. Because of this, image reconstructions often zero-pad acquired k-space data and insert what is equivalent to a sinc-interpolated image into the database. Evaluated here, is an alternative where an acquired-size, complex image is made available to the display and generalized interpolation is used on this data for improved spatial resolution.

Methods

To quantify the overall impact of the interpolation procedures described below, each image is magnified by a factor ranging from 1.1 to 4.0 times the original x and y dimensions in increments of 0.1. For example, a 256x256 image magnified by 1.5 in this experiment will yield a 384x384 image. As MR reconstruction often provides zero-padded DFT-based interpolated images today, this will be used as a standard of reference to compare against.

The first interpolation kernel considered is the four-point cubic spline (1) which, implemented separately, requires eight multiply-adds per pixel of the output image. The second is a generalized interpolation method that involves pre-filtering of the image data, followed by interpolation of the filtered image. From a category of functions that give maximal order interpolation for a minimal amount of support (MOMS) [1], the four-point cubic o-MOMS (2) function is used as the interpolant. The pre-filter applied is specifically designed for use with this interpolant and is well described in [2]. Due to the equivalent support, the compute time for both methods will be the same with exception of the additional pre-filtering step in the o-MOMS processing, which becomes negligible as the size of the magnified image increases.

$$\text{cubic}(x) = \begin{cases} |x|^3 - 2|x|^2 + 1 & 0 \leq |x| < 1 \\ -|x|^3 + 5|x|^2 - 8|x| + 4 & 1 \leq |x| < 2 \end{cases} \quad (1) \quad \text{oMOMS}^3(x) = \begin{cases} \frac{1}{2}|x|^3 - |x|^2 + \frac{1}{14}|x| + \frac{13}{21} & 0 \leq |x| < 1 \\ \frac{-1}{6}|x|^3 + |x|^2 - \frac{85}{42}|x| + \frac{29}{21} & 1 \leq |x| < 2 \end{cases} \quad (2)$$

In addition to the interpolation functions considered above, the impact of performing magnification on the magnitude image versus the magnification of real and imaginary components separately is compared. The interpolation time will take twice as long for this complex case.

Raw data sets were acquired for retrospective reconstruction from a phantom with a radial structure, the ACR phantom (Fig 1a), and a T1-weighted brain. All three data sets have a 256x256 acquisition size, and were collected from a GE Signa HDx 1.5 T scanner with EchoSpeed gradients (GE Healthcare, Waukesha, WI, United States) using a single channel head coil.

Results

For each magnification performed, a measurement was made (3) to evaluate how well the result of an interpolation experiment (g) corresponds to the expected result [2], which in this case is the image from zero-padded interpolation (f). Table 1 contains the mean and standard deviation of this measurement across the range of magnifications (1.1 to 4.0x) for each interpolation type. As shown for the ACR case in Fig 1b and 1c, and consistent across all three images (radial, ACR & brain), using complex data along with generalized interpolation improved the likeness to results from a complex, sinc interpolation. For visual comparison, the ACR phantom resolution holes from a 3.0x magnification are displayed for the complex sinc (Fig 1d), cubic interpolation of magnitude data (Fig 1e), and o-MOMS interpolation of complex data (Fig 1f).

Table 1: 1.1-4.0x magnification results from Eq. 3, in mean (std. dev.)

Interpolation	Radial	ACR	Brain
Cubic (magnitude)	54.6 (0.127)	69.1 (0.256)	61.4 (0.205)
o-MOMS ³ (magnitude)	61.0 (0.034)	71.9 (0.144)	64.7 (0.104)
Cubic (complex)	55.5 (0.139)	75.1 (0.413)	65.7 (0.288)
o-MOMS ³ (complex)	62.9 (0.026)	82.7 (0.137)	72.9 (0.102)

Discussion

Improved magnification of MR images has been demonstrated through higher order interpolation of complex data. While applied in two dimensions for this analysis, the separable interpolation can be used for any number of dimensions of data being magnified.

References

- [1] Blu, et. al. *MOMS: Maximal-Order Interpolation of Minimal Support*. IEEE Transactions on Image Processing 2001; 10:1069-1080.
 [2] Thevenaz, et. al. *Interpolation Revisited*. IEEE Transactions on Medical Imaging; 2000; 19:739-758.

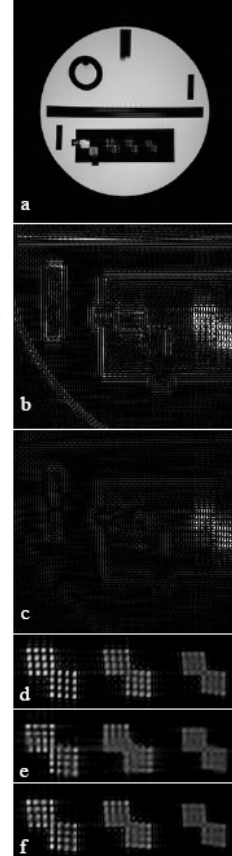


Fig 1: (a)ACR phantom image. Difference of complex sinc 3.0x magnification compared to (b) magnitude cubic, (c) complex oMOMS. ACR Resolution holes after 3.0x zoom of (d) sinc, (e) magnitude cubic, (f) complex oMOMS.

$$10 \log \left(\frac{\sum_{x,y=1}^{\text{len}_{x,y}} f_{x,y}^2}{\sum_{x,y=1}^{\text{len}_{x,y}} (f_{x,y} - g_{x,y})^2} \right) \quad (3)$$



This is to certify that we have examined
this copy of the
master's thesis by

Zachary W. Slavens, B.S.

and have found that it is complete
and satisfactory in all respects.

The thesis has been approved by:

Michael T. Johnson, PhD, Department of Electrical and Computer Engineering

Jason A. Polzin, PhD

James E. Richie, PhD

Approved on _____